# Chapter 6

## RAYLEIGH AND SODIUM LIDAR TECHNIQUES FOR MEASURING MIDDLE ATMOSPHERE DENSITY, TEMPERATURE AND WIND PERTURBATIONS AND THEIR SPECTRA

Chester S. Gardner, Daniel C. Senft, Timothy J. Beatty,
Richard E. Bills and Chris A. Hostetler

Department of Electrical and Computer Engineering
University of Illinois at Urbana-Champaign
1406 West Green Street - Everitt Laboratory
Urbana, IL 61801

## ABSTRACT

We review techniques for measuring middle atmosphere density, temperature and wind perturbations using Rayleigh and Na lidar systems. We restrict our attention to the problem of measuring the mean-square perturbations of these parameters and to the problem of computing relative density and wind spectra. The effects of photon noise on the accuracies of these measurements and the influence of laser power and telescope area on lidar system performance are discussed in detail. Examples of Rayleigh and Na lidar measurements of atmosphere density and temperature profiles and the vertical wavenumber and temporal frequency spectra of relative density and wind perturbations are presented.

## I. INTRODUCTION

The middle atmosphere is a region of complex photochemical and dynamic interaction. Stretching from roughly 30 to 100 km altitude, it is the transition region between the stratosphere and thermosphere and is perhaps the least understood region of the earth's atmosphere. Inaccessible to balloons and satellites, observations of this region must be made by direct *in situ* rocket measurements or by satellite borne or groundbased remote sensing techniques. The middle atmosphere is characterized by a variety of interesting and important features. For example, the temperature minimum at the mesopause near 90 km is the coldest part of the atmosphere. The ionosphere D-region is part of the mesosphere and near 100 km is the turbopause, above which eddy mixing is absent. A variety of layered structures are found in the mesosphere including noctilucent clouds, the polar mesospheric dust layer, the airglow layers and the alkali metal layers of sodium, lithium and potassium.

The density and temperature structure of the middle atmosphere is influenced to a large extent by the effects of gravity waves and tides. Internal gravity waves are believed to be generated primarily by disturbances in the lower atmosphere. Tropospheric convection, storms, wind shears, orographic effects such as airflow over mountains, and even large-scale ocean swells are thought to be common gravity wave sources. These waves propagate through the stratosphere and mesosphere and dissipate their energy near the mesopause making important contributions to the momentum and turbulence budget in this region of the atmosphere. Although the gravity wave wind amplitudes are typically very small in the lower atmosphere, in the absence of dissipation, the velocities grow exponentially with altitude and can approach values as high as 50 m/s at mesopause heights. At these altitudes the waves can change the atmospheric density by as much as 10-20 percent over time periods as short as a few hours. When the amplitudes become too large, instabilities cause the waves to break and dissipate their energy creating turbulence.

The absorption of infrared radiation by $CO_2$ and water vapor in the troposphere and the absorption of UV radiation by ozone in the stratosphere and mesosphere generate atmospheric tides that also propagate through the middle atmosphere. At low- and mid-latitudes, the diurnal (24 h period) and semidiurnal (12 h period) tides appear to have the greatest influence. It is now widely

recognized that both gravity waves and tides play a major role in determining the large-scale circulation and structure of the middle atmosphere [Lindzen, 1981; Fritts, 1984]. Because of their significant influence on density and temperature, the temporal and spatial characteristics of both gravity waves and tides can be studied with Rayleigh and Na lidar techniques.

In this paper we review the techniques for measuring atmospheric density, temperature and wind perturbations using Rayleigh and Na lidar systems. We restrict our attention to the problem of measuring the mean-square perturbations of these parameters and to the problem of computing the density and wind spectra. Several excellent studies of monochromatic gravity waves and tides using lidar techniques have already been published [e.g., Chanin and Hauchecorne, 1981; Batista et al, 1985; Gardner and Voelz, 1987; Kwon et al., 1987; Gardner et al., 1989]. For this reason we concentrate on the effects of the quasi-random waves which are best characterized in terms of spectra and mean-square variations.

The system configurations for typical Rayleigh and Na lidars are briefly described in Section II. The lidar equation and predicted system performance are discussed in Section III and the atmospheric density response to wind perturbations is analyzed in Section IV. The techniques for calculating the mean-square density and horizontal wind perturbations and the associated spatial and temporal spectra are discussed in detail in Section V. The effects of photon noise on the measurements of these parameters are also evaluated in this section. The techniques for calculating temperature profiles from lidar observations are described in Section VI. Practical considerations in processing Rayleigh and Na lidar data are discussed in Section VII. And finally, in Section VIII, example Rayleigh and Na lidar observations of atmospheric density, temperature and wind variations are presented.

This paper was written to provide a reasonably complete description of how to process lidar data for dynamics and temperature studies and how to estimate the accuracies of the measured atmospheric parameters. Some of the sections include considerable mathematical detail which may not be of interest to every reader. For those individuals interested in obtaining a general assessment of the capabilities of both Rayleigh and Na lidars, we recommend reading Sections II and VIII. For those readers interested in understanding the effects of photon noise on the accuracies of the measurements, we recommend reading Sections III, V and VI.

## II. SYSTEM CONFIGURATION

The most common lidar configuration is a monostatic system in which the laser beam is either projected through the receiving telescope or propagates parallel to the optical axis of the telescope. Profile measurements are accomplished by pulsing the laser and range gating the detector. Less common is the bistatic configuration in which the laser and receiving telescope are separated by distances of up to 20 km. Profiling is accomplished by either scanning the telescope along the laser beam or by scanning the laser along the telescope field-of-view. Some of the earliest lidar measurements were conducted by Elterman in the early 1950s. He used a bistatic configuration consisting of a mechanically modulated searchlight and a scanning telescope to measure density and temperature profiles from 10 to 60 km altitude [Elterman, 1951; 1953; 1954]. By modulating the searchlight Elterman was able to discriminate between the scattered signal and the background noise from the stars and moon. Here, we will restrict our discussion to the design of monostatic lidars because they are the most widely used.

The basic design of a monostatic resonance fluorescence lidar system is very similar to the design of aerosol, Rayleigh and Raman lidars. Figure 1 is a block diagram of a typical Na lidar. The pulsed laser is tuned to the $D_2$ resonant absorption line of Na at a wavelength near 589 nm which is in the yellow-orange region of the visible spectrum. Most existing Na lidars employ dye lasers that are pumped by flashlamps, excimer lasers or Nd:YAG lasers. A small fraction (<1 percent) of the output beam is directed to wavelength and energy monitors and to a pulse detector, which triggers the data acquisiton system. The laser pulse propagates up to the Na layer where it is resonantly scattered by neutral Na atoms. The backscattered photons are collected by the telescope and focused onto a photomultiplier tube (PMT). Because the backscattered signal level is very low, the PMT must operate in the photon counting mode even when the lidar system is operated during the daytime. The field stop iris and interference filter in the receiving telescope are designed to reject much of the background light from the stars, moon, and sun. The PMT

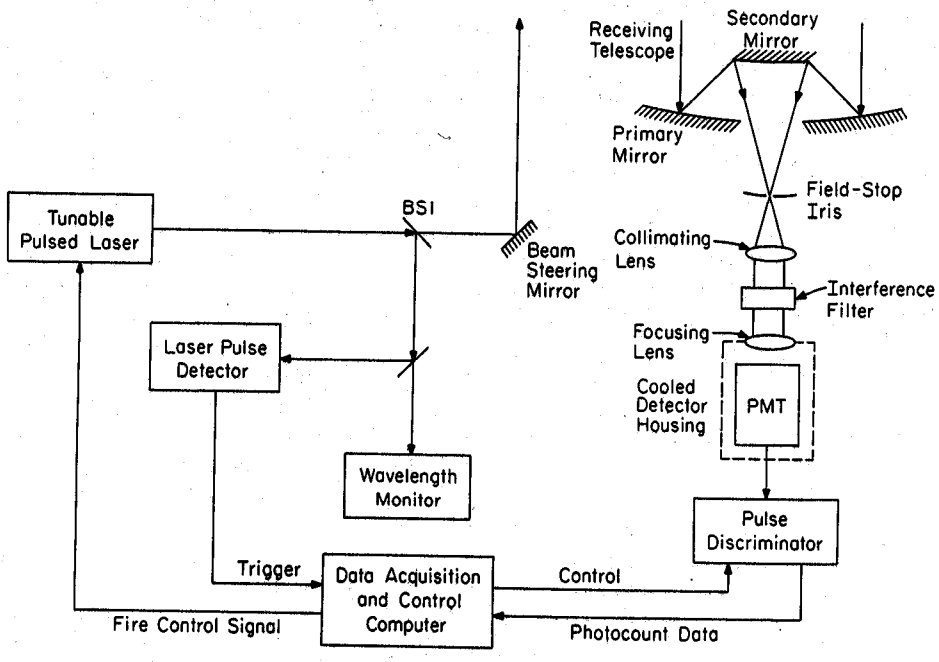


**Figure 1** Block diagram of a typical Na resonance fluorescence lidar system.

signal is processed by a pulse discriminator and range-gated counter. The pulse discriminator converts the low-level (few tenths of a volt) PMT pulses to logic level pulses which can then be counted using conventional high-speed digital circuitry. The raw lidar data consists of a series of photon counts corresponding to consecutive range bins. Because the signal from a single laser pulse is not sufficient to construct a complete Na density profile, the photon counts from many pulses are accumulated over time periods ranging from tens of seconds to several minutes depending on the desired measurement accuracy.

A typical photocount profile is plotted in Fig. 2. This profile was obtained at Arecibo Observatory, Puerto Rico (18°N, 67°W) using the University of Illinois at Urbana-Champaign (UIUC) CEDAR Na lidar. The lidar operated with a 250 ns receiver range-gate which corresponds to a range bin length of 37.5 m. The profile consists of the accumulated photocounts from 4800 laser pulses obtained during an integration period of 25 s. The resonant scattering from the Na layer between about 80 and 105 km is clearly evident. The wavelike structure in the layer is caused by the wind perturbations associated with low-frequency internal gravity waves. The nonzero count level above 110 km is caused primarily by background noise from scattered moonlight and starlight.

The high photocount levels below 60 km result from Rayleigh (i.e., molecular) and Mie scattering by air molecules and aerosols. To prevent overloading by the very strong scattering in the troposphere, the gain of the PMT must be reduced by about 25 dB during the first 50 μs after the laser has fired. The rapid increase in signal level at about 8 km altitude corresponds to the point where the PMT gain is switched to its maximum value. Gain switching can be accomplished either electronically by controlling the PMT gain or mechanically by placing a high-speed rotating shutter wheel near the field stop iris in the telescope. In the UIUC CEDAR lidar system, the gain is switched by controlling the voltage on the first dynode of the PMT.

Because the laser beam propagated beside the telescope, the beam was only partially visible within the telescope field-of-view (FOV) at the lower altitudes. In the absence of dust or aerosol layers, the molecular backscattered signal increases with altitude as the overlap between the laser beam and telescope FOV increases. Eventually the $1/z^2$ (z = altitude) losses and decreasing atmospheric density dominate, the molecular signal level reaches a maximum and then decreases with increasing altitude. For the data plotted in Fig. 2, this occurs at an altitude of about 3 km.

In the troposphere and lower stratosphere, the backscattered signal is often enhanced by Mie scattering from clouds and aerosol layers. Enhanced scattering from aerosol layers at 1, 2 and 5 km can be seen in Fig. 2(b). During the past decade, observations with groundbased and airborne aerosol lidars have provided important information about the dispersion and global distribution of volcanic aerosols [e.g., McCormick et al., 1984; Reiter and Jager, 1986] and about the life cycle and distribution of polar stratospheric clouds (PSC) [e.g., Kent et al., 1986; Iwasaka et al., 1986]. Volcanic aerosols can have a significant influence on climate, while PSCs play a major role in the springtime depletion of ozone over both polar caps. Much of the existing observational data of these phenomena, particularly volcanic aerosols, were obtained with lidars.

Above approximately 25 km and below the Na layer the scattering is purely molecular so that the signal level is proportional to atmospheric density. Rayleigh lidars are designed specifically to measure the molecular scattered signal which can then be used to infer atmospheric density and temperature. The Na lidar Rayleigh signal between 25 and 70 km can be used to study the atmospheric temperature and density profile. The use of high power lasers with the Rayleigh technique was pioneered by Chanin and Hauchecorne [1981]. The data analysis approach is very similar to that employed by Elterman in the early 1950s to measure stratospheric temperatures and is discussed in more detail in Section VI.

## III. LIDAR EQUATION AND SYSTEM PERFORMANCE

The theoretical performance of any lidar system is governed by the lidar equation. The expected received photon count is equal to the product of the system efficiency, number of transmitted photons, probability that a transmitted photon is scattered and probability that a scattered photon is received. For Na resonance fluorescence systems the lidar equation is given approximately by [Gardner et al., 1986]

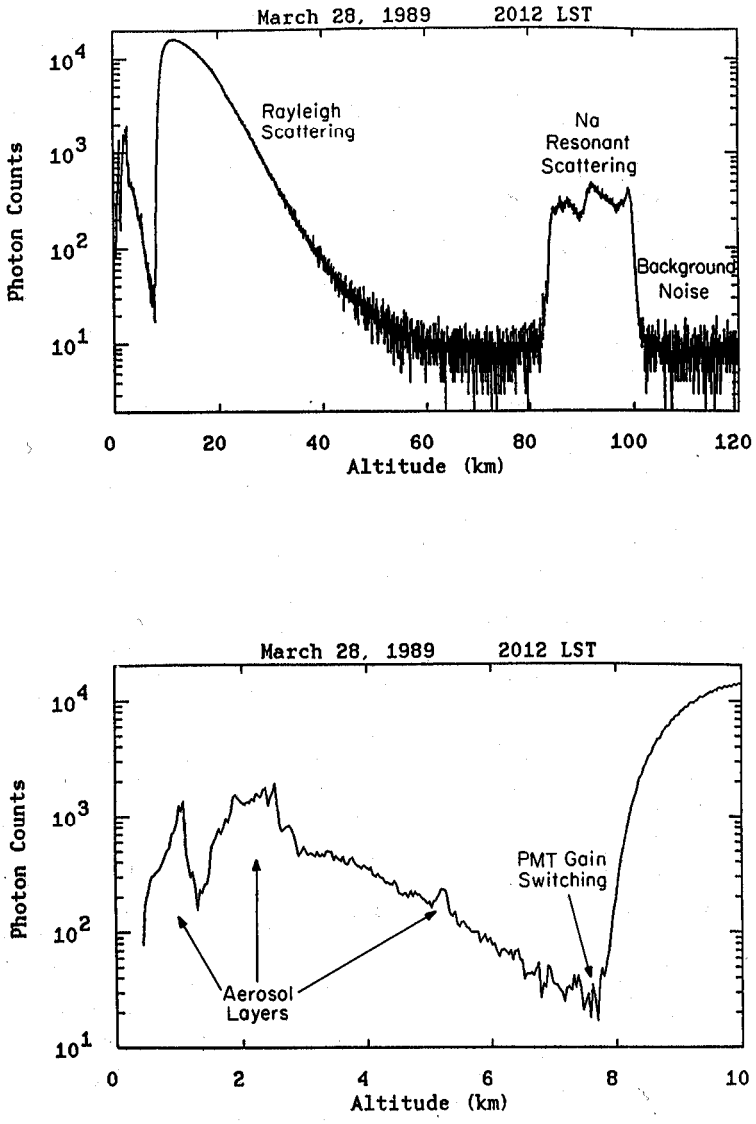


Figure 2 Lidar photon count profile obtained on the night of March 28, 1989 at Arecibo Observatory, Puerto Rico with the UIUC CEDAR Na lidar. The profile was collected by integrating the backscattered signal from 4800 laser shots during a period of 25s starting at 2012 LST. The vertical resolution of the data is 37.5 m. a) Complete profile, b) Expanded low-altitude profile.

$$N_s(z) = \left(\eta T_a^2\right)\left(\frac{P_L \Delta t}{hc/\lambda_L}\right)\left(\sigma_{eff}\, \rho_s(z)\, \Delta z\right)\left(\frac{A_R}{4\pi z^2}\right) + N_B R_L \Delta t \qquad (1)$$

where

$N_s(z)$ = expected number of Na and background photons detected in the range interval $(z - \Delta z/2,\ z + \Delta z/2)$
$\rho_s(z)$ = Na density at range z ($m^{-3}$)
$N_B$ = expected photocount per range bin per pulse due to background noise and dark counts
$\sigma_{eff}$ = effective Na backscatter cross section ($m^2$)
$\Delta z$ = receiver range bin length (m)
$A_R$ = receiving telescope aperture area ($m^2$)
$\lambda_L$ = optical wavelength of laser ($0.589 \times 10^{-6}$ m)
h = Planck's constant ($6.63 \times 10^{-34}$ $Js^{-1}$)
c = velocity of light ($3 \times 10^8$ $ms^{-1}$)
$P_L$ = laser power (w)
$T_a$ = one-way transmittance of the lower atmosphere (z < 80 km)
$R_L$ = laser pulse rate ($s^{-1}$)
$\Delta t$ = integration time (s)
$\eta$ = lidar efficiency

Equation (1) was derived by assuming that extinction of the laser beam as it propagates through the layer is negligible [Simonich and Clemesha, 1983] and that the power densities of the beam within the layer are small enough to ignore the effects of stimulated emission from the excited Na atoms [Welsh and Gardner, 1989]. In practice both of these effects can be significant and should be taken into account when processing Na density data.

The first factor in parenthesis in (1) is the overall system efficiency. The lidar efficiency $\eta$ includes the optical efficiencies of the beam splitters, mirrors, lenses,and optical filters in the laser transmitter and receiving telescope (Fig. 1) as well as the quantum efficiency of the PMT. $\eta$ is dominated by the optical filter transmittance and the detector quantum efficiency. At the Na $D_2$ wavelength, PMTs with GaAs photocathodes have quantum efficiencies between 10 and 20 percent. Wideband optical interference filters with bandwidths greater than 5 Å FWHM typically have transmittances between 30 and 80 percent. Narrowband filters (< 5 Å), which are required for daytime observations, have transmittances of 10 percent or less. Thus, the system efficiencies for well-designed Na lidars range between 1 and 8 percent, with smaller values corresponding to narrowband systems which can operate during day or night. The atmospheric transmittance $T_a$ depends on the wavelength and clarity of the lower atmosphere. Absorption by ozone at near UV wavelengths and by water vapor and carbon dioxide at near IR wavelengths can significantly reduce the atmospheric transmittance. However, under excellent seeing conditions at the Na wavelength, $T_a$ is approximately 80 percent for zenith observations.

The second factor in (1) is the number of transmitted photons. The factor $P_L\Delta t$ is the total laser energy and $hc/\lambda_L$ is the photon energy. The third factor in parenthesis is the probability that a transmitted photon is scattered by a Na atom. The scattering probability is equal to the product of the effective Na backscatter cross section ($\sigma_{eff}$), Na density ($\rho_s(z)$), and the scattering layer thickness ($\Delta z$). The fourth factor is the probability that a scattered photon is collected by the receiving telescope. For isotropic scattering, this probability is equal to the telescope area ($A_R$) divided by the area of a sphere of radius z (i.e., $4\pi z^2$). z is the distance from the scatterer to the telescope. For convenience, effects caused by scattering anisotropies are included in the scattering cross section ($\sigma_{eff}$).

The backscatter cross section depends on the laser wavelength and linewidth and on the velocity and temperature of the scatterer. The Na $D_2$ resonance line is actually a Doppler broadened doublet composed of 6 lines. Figure 3 is a plot of the Na resonance line as a function of wavelength for several values of temperature. As the temperature decreases the minimum between the $D_{2a}$ and $D_{2b}$ lines decreases and the peak intensities of the $D_{2a}$ and $D_{2b}$ lines increase. The backscatter cross section also depends upon the laser linewidth. The maximum value, which is

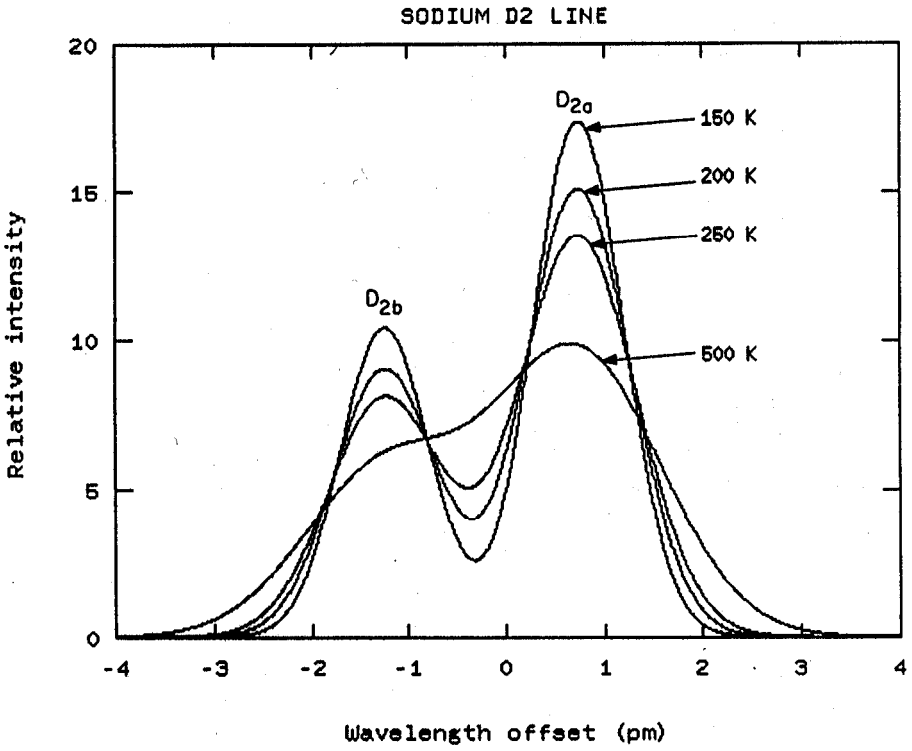


Figure 3 Thermally broadened hyperfine structure of the Na $D_2$ resonance line.

achieved by tuning a narrowband laser (FWHM laser linewidth < 0.5 pm) to the $D_{2a}$ wavelength, is approximately $9.6 \times 10^{-16}$ m$^2$ for T ~ 200 k.

The Na density can be estimated from the photocount data by subtracting the measured background photocount and then solving for $\rho_s(z)$ in (1)

$$\rho_s(z) = \frac{4\pi z^2 hc/\lambda_L}{\eta T_a^2 \sigma_{eff} P_L A_R \Delta z \Delta t} \left[ N_s(z) - \hat{N}_B R_L \Delta t \right] \tag{2}$$

where $\hat{N}_B$ is the estimated photocount per range bin per laser pulse due to background noise and dark counts. Accurate estimates of the background count can be obtained by averaging counts in the range bins above the Na layer.

Because the atmospheric transmittance depends on the clarity of the lower atmosphere and is not easy to measure, the absolute Na density is usually computed by normalizing the Na photocounts by the Rayleigh photocount at an altitude free of aerosols, typically 30-35 km. Aerosol-free regions are relatively easy to identify because the enhanced scattering by aerosols are usually evident in the photocount profiles. Several studies using multi-wavelength lidars have shown that aerosol layers are rare above 35 km and virtually nonexistent above 40 km. The expected photocount at Rayleigh scattering altitudes is given by

$$N_R(z) = \left(\eta T_a^2\right)\left(\frac{P_L \Delta t}{hc/\lambda_L}\right)\left(\sigma_R \rho_a(z) \Delta z\right)\left(\frac{A_R}{4\pi z^2}\right) + N_B R_L \Delta t \tag{3}$$

where

$\rho_a(z)$ = atmospheric density at altitude z (m$^{-3}$)
$\sigma_R$ = Rayleigh backscatter cross secton (m$^2$).

At the Na $D_2$ wavelength $\sigma_R \rho_a$ can be expressed in terms of the atmospheric pressure and temperature

$$\sigma_R \rho_a(z) = 3.539 \times 10^{-6} P(z)/T(z) \tag{4}$$

where $\sigma_R \rho_a$ has units of m$^{-1}$ and

P(z) = atmospheric pressure at altitude z (mbar)
T(z) = atmosphere temperature at altitude z (K).

If $z_R$ is the normalizing altitude, then by using (3) and (4), the Na density can be written as

$$\rho_s(z) = \frac{z^2 \sigma_R \rho_a(z_R)}{z_R^2 \sigma_{eff}} \frac{\left[N_s(z) - \hat{N}_B R_L \Delta t\right]}{\left[N_R(z_R) - \hat{N}_B R_L \Delta t\right]}. \tag{5}$$

The accuracy of the measured Rayleigh photocount can be improved by averaging several range bins above and below $z_R$. However, the atmospheric density decreases approximately exponentially with altitude and to avoid unwanted biases, this characteristic must be taken into account when the average Rayleigh photocount is computed [Gardner et al., 1986].

The required signal level depends on the desired accuracy of the atmospheric parameter being measured. Usually the measurement accuracy can be expressed in terms of the total photocount $N_s$ comprising the Na profile. At mid-latitudes the Na column abundance $C_o$ ranges from a summer minimum of $3 \times 10^9$ cm$^{-2}$ to a winter maximum of about $10^{10}$ cm$^{-2}$. The yearly average value at Urbana, IL (40°N) is approximately $5 \times 10^9$ cm$^{-2}$ [Gardner et al., 1986]. The Na

layer centroid height $z_o$ exhibits a semi-annual oscillation at Urbana with a yearly mean of approximately 92 km. If we use these values in (1), integrate over the altitude of the Na layer and assume $\sigma_{eff} = 9x10^{-16}$ m$^2$, $\eta = 5$ %, and $T_a = 0.7$, then under good seeing conditions we have for the total Na photon count ($N_s$)

$$N_s = \eta T_a^2 \frac{\sigma_{eff} C_o}{4\pi z_o^2 hc/\lambda_L} P_L A_R \Delta t \simeq 3x10^4 P_L A_R \Delta t \quad / \quad (wm^2 s) \tag{6}$$

where the units of $P_L$, $A_R$, and $\Delta t$ are respectively w, m$^2$, and s. If background noise effects are neglected, the measurement errors for the layer density $\rho_s(z)$, column abundance $C_o$, centroid height $z_o$, and rms thickness $\sigma_o$ are given by

$$\mathrm{Std}[\rho_s(z)] \simeq [C_o \rho_s(z)/\Delta z]^{1/2} / \sqrt{N_s}$$

$$\sim 10^{-2} [C_o \rho_s(z)/\Delta z]^{1/2} / \sqrt{P_L A_R \Delta t} \tag{7}$$

$$\mathrm{Std}(C_o) = C_o / \sqrt{N_s} \sim 10^{-2} C_o / \sqrt{P_L A_R \Delta t} \tag{8}$$

$$\mathrm{Std}(z_o) = \sigma_o / \sqrt{N_s} \sim 10^{-2} \sigma_o / \sqrt{P_L A_R \Delta t} \tag{9}$$

$$\mathrm{Std}(\sigma_o) = \sigma_o / \sqrt{2N_s} \sim 10^{-2} \sigma_o / \sqrt{2P_L A_R \Delta t}\,. \tag{10}$$

To obtain accuracies of better than 5 percent for column abundance and better than 200 m for the centroid height and rms thickness, signal levels of approximately 500 counts are required so that $P_L A_R \Delta t \sim 0.05$ wm$^2$s. This level of accuracy can be achieved with a 0.5-w laser, 0.35-m-diameter telescope, and 1-s integration period. Gravity waves typically induce Na density perturbations on the order of 0.1 to 10 percent so that signal levels on the order of $10^4$-$10^5$ counts are required to observe wave induced density fluctuations. To measure accurately gravity wave parameters with a 0.5-w laser and 0.35-m-diameter telescope will require integration periods of 2 to 5 min. It should be noted that in practice the accuracy of the abundance measurement is closer to 10-20 percent because model values for the atmospheric pressure and temperature are typically used in (4) rather than measured values. Notice that measurement accuracies in (7)-(10) are dominated by the factor $P_L A_R \Delta t$. Increased accuracy can only be obtained by increasing the laser power, telescope area, or integration period. Consequently, the relative performance capability of a Na lidar is dictated by the performance factor $P_L A_R$.

The absolute atmospheric density can be estimated from the Rayleigh photocount data by subtracting the measured background count and then normalizing the result by the photocount at an altitude where the absolute density is determined either from an independent observation or from a model atmosphere.

$$\rho_a(z) = \frac{z^2 \rho_a(z_R)}{z_R^2} \frac{\left[N_R(z) - \hat{N}_B R_L \Delta t\right]}{\left[N_R(z_R) - \hat{N}_B R_L \Delta t\right]} \tag{11}$$

The accuracy of the atmospheric density deduced from the Rayleigh backscatter signal is also related to the received photon count levels. Assuming background noise is negligible, the variance of the density estimate is given by

$$\frac{\mathrm{var}[\rho_a(z)]}{\rho_a^2(z)} \simeq \frac{\mathrm{var}[\rho_a(z_R)]}{\rho_a^2(z_R)} + \frac{1}{N_R(z)} \tag{12}$$

where

$$N_R(z) = N_R(z_s)\,(z_s/z)^2\,e^{-(z-z_s)/H} \tag{13}$$

and H is the atmospheric scale height. If we assume $\eta = 5\%$, $T_a = 0.7$, $\lambda_L = 589$ nm and $z_s = 45$ km, then

$$N_R(z_s) \simeq 0.06\,P_L A_R \Delta z \Delta t \;\; / \;\; (wm^2s) \tag{14}$$

and the relative density error caused by photon noise is

$$\frac{\mathrm{Std}\left[\rho_a(z)\right]}{\rho_a(z)} \simeq \frac{1}{\sqrt{N_R(z)}} \simeq \frac{4}{\sqrt{P_L A_R \Delta z \Delta t}}\,(z/z_s)\,e^{(z-z_s)/2H}. \tag{15}$$

In the upper stratosphere the density perturbations caused by gravity waves and tides are typically a few percent or less so that signal levels on the order of $10^5$-$10^6$ counts are required to measure accurately the wave induced density fluctuations. A signal level of $10^5$ counts at 45 km altitude can be achieved by using a 1 m diameter telescope, 10 w laser, 2 min integration period and 1 km vertical resolution.

## IV. ATMOSPHERIC DENSITY RESPONSE TO WIND PERTURBATIONS

Since Rayleigh and Na lidars directly measure density profiles, we are most interested in the affects of waves on the density structure of the atmosphere. In this section we derive equations describing the atmospheric density response to wave induced wind perturbations and then use the results to express the wave parameters in terms of the lidar observations. The density response of the neutral atmosphere or of an atmospheric layer composed of a minor neutral constituent, to wave induced wind perturbations is governed by the continuity equation. By neglecting diffusion and chemical effects and by assuming that the neutral atmosphere or constituent layer is horizontally homogeneous, Gardner and Shelton [1985] have shown that the density response can be written in the form

$$\rho(\underline{r},t) = e^{-\chi}\,\rho_o(z-\xi) \tag{16}$$

where

$\rho(\underline{r},t)$ = perturbed density at position $\underline{r}$ and time t
$\rho_o(z)$ = steady-state density profile in the absence of wind perturbations
$\underline{r} = x\hat{x} + z\hat{z}$ = position vector where x is the horizontal coordinate and z is the vertical coordinate and $\chi$ and $\xi$ are solutions to the partial differential equations

$$\frac{\partial \chi}{\partial t} = \nabla \cdot \underline{V} - \underline{V} \cdot \nabla \chi \tag{17}$$

$$\frac{\partial \xi}{\partial t} = w - \underline{V} \cdot \nabla \xi\,. \tag{18}$$

$\underline{V} = u\hat{x} + w\hat{z}$ is the atmospheric velocity field and u and w are, respectively, the horizontal and vertical velocities. Notice that $\chi$ is related to the wind divergence and $\xi$ is related to the vertical displacement caused by the vertical wind. These two parameters should not be confused with the common notation for geopotential height and vertical gradient of potential temperature.

If the wind perturbations are sufficiently small, the second terms on the right-hand sides of (17) and (18) can be neglected [Gardner and Shelton, 1985] so that

$$\chi(\underline{r},t) \simeq \int_{-\infty}^{t} \nabla\cdot\underline{V}\, d\tau \tag{19}$$

$$\xi(\underline{r},t) \simeq \int_{-\infty}^{t} w\, d\tau\ . \tag{20}$$

In this case the density response is given by

$$\rho(\underline{r},t) \simeq \exp\left(-\int_{-\infty}^{t} \nabla\cdot\underline{V}\, d\tau\right)\rho_o\left(z - \int_{-\infty}^{t} w\, d\tau\right). \tag{21}$$

The density perturbations result from a multiplicative distortion due to the wind divergence and a vertical displacement caused by the vertical winds. The relative importance of these two effects depends on the spatial scale of the wave causing the wind fluctuations.

We are primarily interested in the mean-square values and spectra of the relative density perturbations ($\Delta\rho/\rho$) as a function of time and altitude

$$r(z,t) = \frac{\Delta\rho}{\rho} = \Delta \ln \rho\ . \tag{22}$$

If the unperturbed density profile is modeled as

$$\rho_o(z) = \exp\,[-f(z)]\ , \tag{23}$$

then by using (16) and (22) we have

$$r(z,t) = -\chi - \Delta f(z-\xi) = -\chi - \left[f(z-\xi) - f(z)\right]\ . \tag{24}$$

As a consequence of (24) we can also write

$$\rho(z,t) = \rho_o(z)e^{r(z,t)}\ . \tag{25}$$

By expanding $f(z-\xi)$ in a Taylor series about z and retaining terms out to first order in $\underline{V}$, we obtain

$$r(z,t) \simeq -\chi + \frac{df(z)}{dz}\,\xi\ . \tag{26}$$

Equation (26) is a valid approximation provided

$$|\xi| << |2f'(z)/f''(z)|\ , \tag{27}$$

where the prime denotes differentiation with respect to z.

The hydrostatic equation and ideal gas law (see equations (84) and (85) in Section VI) can be used to relate the atmospheric density and temperature profiles

$$\rho_{oa}(z) = \frac{M}{RT(z)} \exp\left[ - \frac{M}{R} \int_0^z \frac{g(z)}{T(z)}\, dr \right], \tag{28}$$

so that

$$f_a'(z) = \frac{T'(z)}{T(z)} + \frac{Mg(z)}{RT(z)} \tag{29}$$

$$f_a''(z) = \frac{-T''(z)}{T(z)} - \left[\frac{T'(z)}{T(z)}\right]^2 - \frac{Mg(z)}{RT(z)} \frac{T'(z)}{T(z)} \tag{30}$$

where

M = mean molecular weight of the atmosphere = 28.95 kg/kmol
R = universal gas constant = 8314 Nm/(kmol K)
$g(z)$ = gravitational acceleration = $g_o/(1+z/r_o)^2$
$g_o$ = sea level gravitational acceleration = 9.807 m/s$^2$
$r_o$ = mean earth radius = 6357 km .

In the upper stratosphere and lower mesosphere the temperature profile is approximately parabolic with a maximum near the stratopause

$$T(z) \simeq T_s \left[ 1 - \left( \frac{z-z_s}{h_s} \right)^2 \right] \tag{31}$$

where

$T_s$ = stratopause temperature (~ 250K)
$z_s$ = stratopause height (~ 45 km)
$h_s$ = stratopause width (~ 30 km).

By substituting (31) into (29) and (30) we obtain

$$f_a'(z) = \frac{1}{H} - \frac{2(z-z_s)}{h_s^2} \tag{32}$$

$$f_a''(z) = \frac{-2}{h_s^2} + \frac{4(z-z_s)^2}{h_s^4} - \frac{2(z-z_s)}{Hh_s^2} \tag{33}$$

where $H^{-1} = \frac{Mg}{RT_s}$ is the atmospheric scale height at the stratopause. H is approximately 7 km in the upper stratosphere. Equation (27) is easily satisfied in the upper stratosphere and lower mesosphere because the vertical displacements caused by gravity wave winds are typically a few hundred meters or less while $|2f_a'/f_a''|$ is greater than 100 km. Thus, for atmospheric perturbations (26) becomes

$$r_a(z,t) \simeq -\chi + \frac{1}{H}\left[1 - 2H(z-z_s)/h_s^2\right] \xi . \tag{34}$$

It has been shown that a reasonably accurate model for the unperturbed Na layer is a Gaussian profile [Gardner and Voelz, 1987]

$$\rho_{os}(z) = \frac{C_o}{\sqrt{2\pi}\,\sigma_o} \exp\left[ - \frac{(z-z_o)^2}{2\sigma_o^2} \right] \tag{35}$$

where

$C_o$ = Na column abundance
$z_o$ = layer centroid height
$\sigma_o$ = rms layer width.

In this case $f_s(z)$ for the Na layer is quadratic so that (26) becomes

$$r_s(z,t) = - \chi + \frac{(z-z_o)}{\sigma_o^2} \xi \, . \tag{36}$$

When the density perturbations are caused by gravity waves, it is possible to simplify (34) and (36). If the vertical wavelength $\lambda_z$ and intrinsic frequency $\omega$ satisfy the conditions $\lambda_z << 4\pi H$ and $\omega << N$ where N is the buoyancy frequency, the gravity wave polarization and dispension relations can be used to show that [Gardner and Shelton, 1985]

$$\xi = \gamma H \chi \, . \tag{37}$$

$\gamma$ is the ratio of specific heats. In this case the relative density perturbations can be written as

$$r_a(z,t) = \frac{(\gamma-1)}{\gamma H} \left[ 1 - \frac{2\gamma H (z-z_s)}{h_s^2} \right] \xi \quad \text{(atmosphere)} \tag{38}$$

$$r_s(z,t) = \frac{-1}{\gamma H} \left[ 1 - \frac{\gamma H (z-z_o)}{\sigma_o^2} \right] \xi \, . \quad \text{(Na layer)} \tag{39}$$

It is convenient to express the relative Na density perturbations in terms of the relative atmospheric density perturbations. Equation (38) is valid for the region near the stratopause. A similar expression, valid near the mesopause, can be derived by noting that the temperature profile is also approximately parabolic in the mesopause region

$$T(z) \simeq T_m \left[ 1 + \left( \frac{z-z_m}{h_m} \right)^2 \right] \tag{40}$$

where

$T_m$ = mesopause temperature
$z_m$ = mesopause height (~ 90 km)
$h_m$ = mesopause width (~ 30 km).

As a consequence of (26), (29) and (40) we have

$$r_a(z,t) = \frac{(\gamma-1)}{\gamma H} \left[ 1 + \frac{2\gamma H (z-z_m)}{h_m^2} \right] \xi \, . \tag{41}$$

The Na layer is centered approximately at the mesopause and the full-width at the $e^{-2}$ points is only about 20 km. Consequently, in the region of the Na layer, the second term on the right hand side of (41) is negligible so that (39) can be written as

$$r_s(z,t) \simeq \frac{-1}{(\gamma-1)} \left[ 1 - \frac{\gamma H(z-z_o)}{\sigma_o^2} \right] r_a(z,t) \,. \tag{42}$$

By using (42) the mean-square Na density perturbations can be expressed in terms of the mean-square atmospheric density fluctuations.

$$\langle r_s^2(z,t) \rangle = \left[ 1 - \gamma H(z-z_o)/\sigma_o^2 \right]^2 \langle r_a^2(z,t) \rangle / (\gamma-1)^2 \,. \tag{43}$$

The vertical wavenumber and temporal frequency spectra of the atmospheric and Na density perturbations can also be related using (42). For the temporal spectrum we have

$$\frac{\langle |R_a(z,\omega)|^2 \rangle}{T} = F_a(\omega) \tag{44}$$

$$\frac{\langle |R_s(z,\omega)|^2 \rangle}{T} = \frac{\left[ 1-\gamma H(z-z_o)/\sigma_o^2 \right]^2}{(\gamma-1)^2} \, F_a(\omega), \tag{45}$$

where $R_a$ and $R_s$ are respectively the temporal Fourier transforms of $r_a$ and $r_s$.

$$R_a(z,\omega) = \int_0^T r_a(z,t) \, e^{i\omega t} \, dt \tag{46}$$

$$R_s(z,\omega) = \int_0^T r_s(z,t) \, e^{i\omega t} \, dt \tag{47}$$

$F_a(\omega)$ is the atmospheric density perturbation spectrum and T is the observation period. If the vertical extent of the Na layer L is large compared to the vertical correlation length of the density or wind perturbations, then the vertical wavenumber spectra of the Na and atmospheric density fluctuations are also related,

$$\frac{\langle |R_a(k_z,t)|^2 \rangle}{L} = F_a(k_z) \tag{48}$$

$$\frac{\langle |R_s(k_z,t)|^2 \rangle}{L} \simeq \frac{1}{\mu^2} \, F_a(k_z) \tag{49}$$

where

$$\mu^2 = \frac{(\gamma-1)^2}{\left[ 1+(\gamma HL/\sigma_o^2)^2/12 \right]} \tag{50}$$

and

$$R_a(k_z,t) = \int_{z_o-L/2}^{z_o+L/2} r_a(z,t)\, e^{ik_z z}\, dz \tag{51}$$

$$R_s(k_z,t) = \int_{z_o-L/2}^{z_o+L/2} r_s(z,t)\, e^{ik_z z}\, dz\ . \tag{52}$$

Although Rayleigh and Na lidars measure density, the gravity wave polarization and dispersion relations can be used to relate the mean-square atmospheric density perturbations $(\langle r_a^2\rangle = \langle(\Delta\rho_a/\rho_a)^2\rangle)$ and density power spectra ($F_a$) to the mean-square horizontal wind perturbations $(\langle u^2\rangle)$ and horizontal wind power spectra ($F_u$).

$$\langle u^2(z,t)\rangle \simeq (g/N)^2 \langle r_a^2(z,t)\rangle = (g/N)^2 \left\langle \left[\frac{\Delta\rho_a(z,t)}{\rho_a(z,t)}\right]^2 \right\rangle \tag{53}$$

$$F_u(k_z) \simeq (g/N)^2\, F_a(k_z) \tag{54}$$

$$F_u(\omega) \simeq (g/N)^2\ F_a(\omega) \tag{55}$$

## V. ANALYSIS OF LIDAR DENSITY DATA FOR DYNAMICS STUDIES

In this section, we discuss the problem of estimating the mean-square atmospheric density fluctuations and spectra from the Rayleigh and Na lidar data. Because the parameters $r_a$ and $r_s$ are derived from photon count profiles, they will be contaminated by shot noise. The statistical fluctuations of the photon counts establish noise floors in the power spectra and bias terms in the computed mean-square density variations which are inversely proportional to the signal count. Photon noise will also introduce random errors into the measured values of the spectra and mean-square density variations. The variances of these parameters will also be inversely related to the signal count. In many cases the noise floors, bias terms and variances can be reduced substantially by spatially and temporally filtering the photocount data.

The temporal variations of the Rayleigh photon count $N_R$ caused by wave affects are typically very small. In the following analysis we assume for simplicity that $N_R$ is constant with respect to time. If photon noise effects are included, the mean-square value of $r_a$ is given by

$$\langle r_a^2(z,t)\rangle = \left\langle \left[\frac{\Delta\rho_a(z,t)}{\rho_a(z,t)}\right]^2 \right\rangle + \frac{1}{N_R(z)}\ . \tag{56}$$

The first term on the right-hand side of (56) is the mean-square atmospheric density fluctuations and the second term is the contribution due to photon noise. Recall the $N_R(z)$ is the photon count per profile in the range bin corresponding to altitude z. This photon noise bias term can be reduced substantially by spatially and temporally filtering $r_a$. Low-pass filtering increases the effective photon count because the process is equivalent to summing the counts over several adjacent range bins and profiles. Assume the filters are ideal low-pass filters with spatial and temporal cutoff frequencies given by

$$k_c = 2\pi/\lambda_c \le \pi/\Delta z \tag{57}$$

$$\omega_c = 2\pi/T_c \le \pi/\Delta t \tag{58}$$

where $\lambda_c$ is the cutoff wavelength and $T_c$ is the cutoff period. The upper limits on the cutoff frequencies given in (57) and (58) are established by the Nyquist sampling criterion. If the bandwidths of these filters are larger than the bandwidths of the atmospheric density fluctuations, then after filtering the mean-square value of $r_a$ is

$$\langle r_a^2(z,t)\rangle \simeq \left\langle \left[\frac{\Delta\rho_a(z,t)}{\rho_a(z,t)}\right]^2 \right\rangle + \frac{4\Delta z\Delta t}{\lambda_c T_c N_R(z)} . \tag{59}$$

In processing the lidar data, ensemble averages must be approximated by computing either spatial or temporal averages or a combination of both. The mean-square density perturbations as a function of altitude can be estimated by averaging $r_a^2$ over the observation period. The expected value ($\langle\bullet\rangle$) of the temporal average is

$$\frac{1}{T}\int_0^T \langle [r_a(z,t) - \bar{r}_a(z)]^2 \rangle \, dt = \left\langle \left[\frac{\Delta\rho_a(z)}{\rho_a(z)}\right]^2 \right\rangle + \frac{4\Delta z\Delta t}{\lambda_c T_c N_R(z)} \tag{60}$$

$$\bar{r}_a(z) = \frac{1}{T}\int_0^T r_a(z,t)dt \tag{61}$$

The value of the density perturbations calculated using (60) includes the affects of all waves with periods between $T_c$ and T and vertical wavelengths greater than $\lambda_c$. The effects of waves with vertical wavelengths greater than $\lambda_o$ can be eliminated if $\bar{r}_a$ and $(r_a-\bar{r}_a)^2$ are also averaged over the height range $(z-\lambda_o/2,\ z+\lambda_o/2)$. In this case the calculated density perturbations will include the effects of all waves with periods between $T_c$ and T and vertical wavelengths between $\lambda_c$ and $\lambda_o$.

Similarly, the temporal variations of the mean-square density perturbations can be estimated by averaging $r_a^2$ over the altitude range of observations. The expected value ($\langle\bullet\rangle$) of the spatial average is

$$\frac{1}{L}\int_{z_s-L/2}^{z_s+L/2} \langle [r_a(z,t) - \bar{r}_a(t)]^2 \rangle \, dz = \left\langle \left[\frac{\Delta\rho_a(t)}{\rho_a(t)}\right]^2 \right\rangle + \frac{4\Delta z\Delta t}{\lambda_c T_c}\frac{1}{L}\int_{z_s-L/2}^{z_s+L/2}\frac{dz}{N_R(z)} \tag{62}$$

$$\bar{r}_a(t) = \frac{1}{L}\int_{z_s-L/2}^{z_s+L/2} r_a(z,t)\, dz . \tag{63}$$

The density perturbations calculated using (62) include the effects of all waves with periods greater than $T_c$ and vertical wavelengths between $\lambda_c$ and L. If $\bar{r}_a$ and $(r_a-\bar{r}_a)^2$ are also averaged over the period $(t-T_o/2,\ t+T_o/2)$, the calculated value of mean-square density perturbations will include the affects of all waves with periods between $T_c$ and $T_o$ and vertical wavelengths between $\lambda_c$ and L.

The corresponding results for the mean-square atmospheric density fluctuations, calculated from the Na density data are

$$\frac{(\gamma-1)^2}{\left[1-\gamma H(z-z_o)/\sigma_o^2\right]^2}\frac{1}{T}\int_0^T \left\langle \left[r_s(z,t) - \bar{r}_s(z)\right]^2 \right\rangle dt =$$

$$<\left[\frac{\Delta\rho_a(z)}{\rho_a(z)}\right]^2> + \frac{(\gamma-1)^2}{\left[1-\gamma H(z-z_o)/\sigma_o^2\right]^2}\,\frac{4\Delta z\Delta t}{\lambda_c T_c N_s(z)} \tag{64}$$

$$\frac{\mu^2}{L}\int_{z_o-L/2}^{z_o+L/2} <\left[r_s(z,t)-\bar{r}_s(t)\right]^2> dz = <\left[\frac{\Delta\rho_a(t)}{\rho_a(t)}\right]^2>$$

$$+\frac{4\Delta z\Delta t}{\lambda_c T_c}\,\frac{\mu^2}{L}\int_{z_o-L/2}^{z_o+L/2}\frac{dz}{N_s(z)} \tag{65}$$

where

$$\bar{r}_s(z) = \frac{1}{T}\int_0^T r_s(z,t)\,dt \tag{66}$$

$$\bar{r}_s(t) = \frac{1}{L}\int_{z_o-L/2}^{z_o+L/2} r_s(z,t)\,dt\ . \tag{67}$$

Notice that at the altitude $z_1 = z_o + \sigma_o^2/\gamma H$, the multiplicative factor on the left-hand side of (64) becomes infinite. This is the altitude at which first-order wave effects (i.e., effects related to $\underline{V}$) have no influence on the Na profile [Gardner and Shelton, 1985]. In the vicinity of this altitude, the calculations in (64) are very sensitive to noise so that the atmospheric density fluctuations cannot be estimated accurately. Because $\sigma_o$ is nominally 4.25 km and H is approximately 6 km at the mesopause, $z_1$ is typically 2.4 km above the layer centroid height or about 95 km.

The appropriate cutoff frequencies for filtering $r_a$ or $r_s$ can be determined by computing the power spectra of the atmospheric density fluctuations. The statistical fluctuations of the photon counts establish noise floors in the spectra which are inversely proportional to the signal count. The noise floors in the temporal power spectra can be reduced by first spatially low-pass filtering $r_a$ and $r_s$. If photon noise effects are included and the temporal spectra of $r_a$ are computed at each altitude in the Rayleigh region according to (44) and (46) and then averaged, we have for the expected value (<•>) of the spatial average

$$\frac{1}{L}\int_{z_s-L/2}^{z_s+L/2}\frac{<|R_a(z,\omega)|^2>}{T}\,dz = F_a(\omega) + \frac{2\Delta z\Delta t}{\lambda_c}\,\frac{1}{L}\int_{z_s-L/2}^{z_s+L/2}\frac{dz}{N_R(z)}\ . \tag{68}$$

Similarly, if the spectra of $r_s$ are computed throughout the Na layer according to (45) and (47) and then averaged, we obtain

$$\frac{\mu^2}{L}\int_{z_o-L/2}^{z_o+L/2}\frac{<|R_s(z,\omega)|^2>}{T}\,dz \simeq F_a(\omega) + \frac{2\Delta z\Delta t}{\lambda_c}\,\frac{\mu^2}{L}\int_{z_o-L/2}^{z_o+L/2}\frac{dz}{N_s(z)}\ . \tag{69}$$

Equations (68) and (69) were derived by assuming that $r_a$ and $r_s$ were low-pass filtered spatially with a cut-off wavelength $\lambda_c$ before the spectra were computed. The corresponding results for the vertical wave number spectra computed from each profile according to (48)-(52) and then averaged over the observation period are

$$\frac{1}{T}\int_0^T \frac{\langle |R_a(k_z,t)|^2\rangle}{L}\,dt \simeq F_a(k_z) + \frac{2\Delta z\Delta t}{T_c}\,\frac{1}{L}\int_{z_s-L/2}^{z_s+L/2}\frac{dz}{N_R(z)} \tag{70}$$

$$\frac{\mu^2}{T}\int_0^T \frac{\langle |R_s(k_z,t)|^2\rangle}{L}\,dt \simeq F_a(k_z) + \frac{2\Delta z\Delta t}{T_c}\,\frac{\mu^2}{L}\int_{z_s-L/2}^{z_s+L/2}\frac{dz}{N_s(z)}\,. \tag{71}$$

Equations (70) and (71) were derived by assuming that $r_a$ and $r_s$ were low-pass filtered temporally with a cut-off period $T_c$ before the spectra were computed.

The bias terms and noise floors all depend inversely on the count levels. If we assume that the atmospheric density profile is approximately exponential and the Na density profile is approximately Gaussian, then

$$N_R(z) \simeq N_R(z_s)\,(z_s/z)^2\,e^{-(z-z_s)/H} \tag{72}$$

$$N_s(z) \simeq \frac{N_s\Delta z}{\sqrt{2\pi}\sigma_o}\,e^{-(z-z_o)^2/2\sigma_o^2} \tag{73}$$

and

$$\frac{1}{L}\int_{z_s-L/2}^{z_s+L/2}\frac{dz}{N_R(z)} \simeq \frac{H}{LN_R(z_s)}\left(1+\frac{L/2-H}{z_s}\right)^2 e^{L/2H} \tag{74}$$

$$\frac{1}{L}\int_{z_o-L/2}^{z_o+L/2}\frac{dz}{N_s(z)} \simeq \frac{\sqrt{2\pi}\sigma_o}{N_s\Delta z}\sum_{n=0}^{\infty}\left(\frac{L}{2\sqrt{2}\sigma_o}\right)^{2n}\Big/(2n+1)n!$$

$$\simeq \frac{4\sqrt{2\pi}\sigma_o}{N_s\,\Delta z}\,. \tag{75}$$

In (75) we have assumed that L is the altitude range over which the Na density is greater than 5 percent of the peak density. In this case, L is approximately 20 km. $N_s$ and $N_R(z_s)$ are evaluated for typical system parameters in equations (6) and (14), respectively.

The statistical fluctuations of the photon counts will also contribute random errors to the measured values of the density perturbations and spectra. The variances of $\langle(\Delta\rho_a/\rho_a)^2\rangle$ and $E_a$ caused by photon noise are similar in form to the bias terms and photon noise floors and are inversely proportional to the signal counts. The biases and variances of the computed mean-square atmospheric density fluctuations are summarized in Table I. The noise floors and variances of the computed atmospheric density spectra are summarized in Table II. In all cases, the bias terms, noise floors and variances are inversely proportional to the lidar performance factor $P_L A_R$. Notice

**Table I**
**Summary of Bias Terms and Variances of the Computed Values of the Mean-Square Relative Atmospheric Density Fluctuations**

| Lidar Type | Mean-Square Relative Density | Bias Term* | Mean-Square Relative Density Variance |
|---|---|---|---|
| Rayleigh | $<\left[\frac{\Delta\rho_a(z)}{\rho_a(z)}\right]^2>$ | $\frac{4\Delta z\Delta t}{\lambda_c T_c N_R(z)} \sim \frac{70}{P_L A_R \lambda_c T_c}(z/z_s)^2 e^{(z-z_s)/H}$ | $<\left[\frac{\Delta\rho_a(z)}{\rho_a(z)}\right]^2> \frac{8\Delta z\Delta t}{\lambda_c T N_R(z)}$ |
| Rayleigh | $<\left[\frac{\Delta\rho_a(t)}{\rho_a(t)}\right]^2>$ | $\frac{4\Delta z\Delta t}{\lambda_c T_c}\frac{1}{L}\int_{z_s-L/2}^{z_s+L/2}\frac{dz}{N_R(z)} \sim \frac{200}{P_L A_R \lambda_c T_c}$ | $<\left[\frac{\Delta\rho_a(t)}{\rho_a(t)}\right]^2> \frac{8\Delta z\Delta t}{L\,T_c}\frac{1}{L}\int_{z_s-L/2}^{z_s+L/2}\frac{dz}{N_R(z)}$ |
| Na | $<\left[\frac{\Delta\rho_a(z)}{\rho_a(z)}\right]^2>$ | $\frac{4\Delta z\Delta t}{\lambda_c T_c N_s(z)}\frac{(\gamma-1)^2}{\left[1-\gamma H(z-z_o)/\sigma_o^2\right]^2} \sim \frac{0.2}{P_L A_R \lambda_c T_c}\frac{e^{(z-z_o)^2/2\sigma_o^2}}{\left[1-\gamma H(z-z_o)/\sigma_o^2\right]^2}$ | $<\left[\frac{\Delta\rho_a(z)}{\rho_a(z)}\right]^2> \frac{8\Delta z\Delta t}{\lambda_c T N_s(z)}\frac{(\gamma-1)^2}{\left[1-\gamma H(z-z_o)/\sigma_o^2\right]^2}$ |
| Na | $<\left[\frac{\Delta\rho_a(t)}{\rho_a(t)}\right]^2>$ | $\frac{4\Delta z\Delta t}{\lambda_c T_c}\frac{\mu^2}{L}\int_{z_o-L/2}^{z_o+L/2}\frac{dz}{N_s(z)} \sim \frac{0.1}{P_L A_R \lambda_c T_c}$ | $<\left[\frac{\Delta\rho_a(t)}{\rho_a(t)}\right]^2> \frac{8\Delta z\Delta t}{L\,T_c}\frac{\mu^2}{L}\int_{z_o-L/2}^{z_o+L/2}\frac{dz}{N_s(z)}$ |

* For Rayleigh lidar data, bias terms were calculated assuming $z_s = 45$ km, $L = 30$ km and $H = 7$ km.
For Na lidar data, bias terms were calculated assuming $\sigma_o = 4.25$ km, $L = 20$ km and $H = 6$ km.
In both cases, it was assumed $\eta = 5\%$, $T_a = 0.7$ and $\lambda_L = 589$ nm.
For the bias terms the parameter units are $P_L$(w), $A_R$($m^2$), $\lambda_c$(m) and $T_c$(s).

**Table II**
**Summary of Noise Floors and Variances of the Computed Spectra of the Relative Atmospheric Density Fluctuations**

| Lidar Type | Relative Density Spectrum | Noise Floor* | Spectrum Variance |
|---|---|---|---|
| Rayleigh | $F_a(k_z)$ | $\frac{2\Delta z\Delta t}{T_c}\frac{1}{L}\int_{z_s-L/2}^{z_s+L/2}\frac{dz}{N_R(z)} \sim \frac{100}{P_L A_R T_c}$ (m) | $F_a(k_z)\frac{2\Delta z\Delta t}{T}\frac{1}{L}\int_{z_s-L/2}^{z_s+L/2}\frac{dz}{N_R(z)}$ |
| Rayleigh | $F_a(\omega)$ | $\frac{2\Delta z\Delta t}{\lambda_c}\frac{1}{L}\int_{z_s-L/2}^{z_s+L/2}\frac{dz}{N_R(z)} \sim \frac{100}{P_L A_R \lambda_c}$ (s) | $F_a(\omega)\frac{2\Delta z\Delta t}{L}\frac{1}{L}\int_{z_s-L/2}^{z_s+L/2}\frac{dz}{N_R(z)}$ |
| Na | $F_a(k_z)$ | $\frac{2\Delta z\Delta t}{T_c}\frac{\mu^2}{L}\int_{z_o-L/2}^{z_o+L/2}\frac{dz}{N_s(z)} \sim \frac{0.05}{P_L A_R T_c}$ (m) | $F_a(k_z)\frac{2\Delta z\Delta t}{T}\frac{\mu^2}{L}\int_{z_o-L/2}^{z_o+L/2}\frac{dz}{N_s(z)}$ |
| Na | $F_a(\omega)$ | $\frac{2\Delta z\Delta t}{\lambda_c}\frac{\mu^2}{L}\int_{z_o-L/2}^{z_o+L/2}\frac{dz}{N_s(z)} \sim \frac{0.05}{P_L A_R \lambda_c}$ (s) | $F_a(\omega)\frac{2\Delta z\Delta t}{L}\frac{\mu^2}{L}\int_{z_o-L/2}^{z_o+L/2}\frac{dz}{N_s(z)}$ |

* Noise floors were calculated using the same parameter values listed in Table I.
For the noise floors the parameter units are $P_L$(w), $A_R$($m^2$), $\lambda_c$(m) and $T_c$(s).

that for comparable performance factors, these parameters for the Na data are approximately 3 orders of magnitude smaller than the corresponding values for the Rayleigh data. This performance advantage for Na lidars is a consequence of the large resonant backscatter cross-section for Na and the large density gradients on the bottom- and top-sides of the layer which enhance the wind induced density perturbations. Na lidars have an additional advantage because the atmospheric density fluctuations are usually much larger near the mesopause compared to the stratopause. However, the most powerful Na lasers available today can only achieve power levels ~5 w compared to 50 w for the near-UV excimer lasers which are beginning to be used for larger Rayleigh lidars. Ths most powerful Na lidars currently in operation have performance factors in the range of 5-10 $wm^2$ compared to almost 100 $wm^2$ for the most powerful Rayleigh lidars. From a scientific standpoint, performance comparisons between the two techniques are largely irrelevant since Rayleigh and Na lidars make observations in different but equally important atmospheric regions.

Because the relative atmospheric density fluctuations range from at most a few percent in the upper stratosphere to 5-15 percent near the mesopause, the bias terms should be smaller than $10^{-4}$ to insure accurate estimates of the mean-square density fluctuations. This condition requires

$$P_L A_R \lambda_c T_c > 10^6 \text{ wm}^3\text{s} \qquad \text{(Rayleigh lidars)} \tag{76}$$

$$P_L A_R \lambda_c T_c > 10^3 \text{ wm}^3\text{s} \qquad \text{(Na lidars)}. \tag{77}$$

For a Rayleigh lidar with $P_L$ = 10 w and $A_R$ = 1 $m^2$, this condition can be met by low-pass filtering the data using a cutoff period of 100 s and a cutoff wavelength of 1 km. For a Na lidar with $P_L$ =1 w and $A_R$ = 1 $m^2$, this condition can be met by filtering using a 10 s cutoff period and a 100 m cutoff wavelength.

In recent years, experimental data and theoretical arguments have suggested that there is a universal form for the vertical wavenumber spectrum of horizontal wind perturbations in the upper atmosphere [Dewan and Good, 1986; Smith et al., 1989]. The theoretical horizontal wind spectrum is

$$F_u(k_z) \sim \frac{N^2}{2k_z^3}. \tag{78}$$

The theoretical spectrum for the atmospheric density fluctuations can be derived using (54) and (78)

$$F_a(k_z) \sim \left(\frac{\gamma\text{-}1}{\gamma H}\right)^2 \frac{1}{2k_z^3}. \tag{79}$$

At a vertical wavelength of 1 km, (79) gives a value of approximately $5\text{x}10^{-3}$ m for the density spectrum. For a lidar to observe reliably the spectrum out to a spatial frequency of 1 $km^{-1}$, the noise floors must be less than $5\text{x}10^{-3}$ m which requires (see Table II)

$$P_L A_R T_c > 2\text{x}10^4 \text{ wm}^2\text{s} \qquad \text{(Rayleigh lidars)} \tag{80}$$

$$P_L A_R T_c > 10 \text{ wm}^2\text{s} \qquad \text{(Na lidars)}. \tag{81}$$

This criterion can be satisfied by a Rayleigh lidar with $P_L$ = 10 w, $A_R$ = 1 $m^2$ and $T_c$ = 30 min or a Na lidar with $P_L$ = 1 w, $A_R$ = 1 $m^2$ and $T_c$ = 10 s.

No theoretical models have yet been developed for the gravity wave temporal spectrum. However, radar and lidar observations in the mesosphere indicate that at the buoyancy frequency (~ 0.2 $min^{-1}$), the magnitude of the wave spectrum is typically of the order of $10^3$ - $10^4$ $m^2s^{-1}$. According to (55), this level corresponds to a density spectrum value of $5\text{x}10^{-3}$ - $5\text{x}10^{-2}$ s. Thus,

to observe reliably the temporal spectrum out to the buoyancy frequency, the noise floors must be less than $5 \times 10^{-3}$ s which requires (see Table II)

$$P_L A_R \lambda_c > 2 \times 10^4 \text{ wm}^3 \qquad \text{(Rayleigh lidars)} \tag{82}$$

$$P_L A_R \lambda_c > 10 \text{ wm}^3 \qquad \text{(Na lidars)}. \tag{83}$$

This criterion can be met by a Raleigh lidar with $P_L = 10$ w, $A_R = 1$ m$^2$ and $\lambda_c = 2$ km or a Na lidar with $P_L = 1$ w, $A_R = 1$ m$^2$ and $\lambda_c = 10$ m.

## VI. ANALYSIS OF LIDAR DENSITY DATA FOR TEMPERATURE STUDIES

Both Rayleigh and Na lidars can be used to measure atmospheric temperature profiles. The Rayleigh technique was pioneered by Elterman [1951, 1953 and 1954] in the early 1950s. The temperature profile is inferred from the relative atmospheric density profile by using the hydrostatic equation and the ideal gas law. The Na technique was first demonstrated in the late 1970s by Gibson et al. [1979]. Na temperature is inferred by observing the thermally broadened hyperfine structure of the $D_2$ emission line with a narrowband laser. In this section, we discuss the problem of estimating the atmospheric temperature profile from the Rayleigh and Na lidar data. The impact of signal photon noise on the accuracies of the inferred temperatures is evaluated.

Rayleigh lidars measure the relative atmospheric density profile. To determine temperature from these measurements, the density profile is integrated downward using the hydrostatic equation, ideal gas law and an assumed upper level temperature. The initial upper level temperature may be chosen from a model because when the equation has been integrated downward by about one and one-half scale heights, the calculated temperature is relatively insensitive to the initial estimate. The hydrostatic equation

$$dP = - \rho_a g \, dz \tag{84}$$

can be combined with the ideal gas law

$$P = \rho_a RT/M \tag{85}$$

and integrated to yield

$$T(z) = \frac{T(z_1)\, \rho_a(z_1)}{\rho_a(z)} + \frac{M}{R} \int_z^{z_1} \frac{g(r) \rho_a(r)}{\rho_a(z)} \, dr \tag{86}$$

where

$T(z)$ = atmospheric temperature profile (K)
$P(z)$ = atmospheric pressure profile (mbar)
$\rho_a(z)$ = atmospheric density profile ($m^{-3}$)
$z_1$ = altitude of upper level temperature estimate (m).

Notice that the atmospheric density appears as a ratio of densities in (86). Thus, to determine temperature it is only necessary to measure the relative density. The accuracy of this technique depends upon the molecular or Rayleigh photocount $N_R(z)$ and the accuracy of the upper level temperature estimate $T(z_1)$. Accuracy can be improved substantially by low-pass filtering the photocount data. When filtering the data spatially, care must be taken to insure that the filtering process does not distort the atmospheric density profile. The most effective approach is to filter

$r_a(z,t)$ rather than the photocount profiles. In this case the relative atmospheric density profile is estimated from the filtered values of $r_a$ using (25). If $r_a$ is filtered using ideal low-pass spatial and temporal filters, then the variance of the inferred temperature profile is

$$\mathrm{var}[T(z)] \simeq \frac{4\Delta z\Delta t}{\lambda_c T_c}\,\frac{T^2(z)}{N_R(z)} + \left\{\mathrm{var}[T(z_1)] + \frac{4\Delta z\Delta t}{\lambda_c T_c}\,\frac{T^2(z_1)}{N_R(z_1)}\right\}\exp[-2(z_1-z)/H]. \tag{87}$$

Notice that the error is inversely proportional to the photon count. For altitudes well below $z_1$, the standard deviation of the temperature measurement is

$$\mathrm{Std}[T(z)] \simeq \left[\frac{4\Delta z\Delta t}{\lambda_c T_c N_R(z)}\right]^{1/2} T(z) \sim \frac{8T(z)}{\sqrt{P_L A_R \lambda_c T_c}}\,(z/z_s)e^{(z-z_s)/2H}. \tag{88}$$

Near the stratopause the temperature is approximately 270 K. To achieve a measurement accuracy of 1 K at $z=z_s$ requires

$$P_L A_R \lambda_c T_c \gtrsim 5\times10^6\ \mathrm{wm^3s}. \tag{89}$$

This accuracy can be achieved by using a lidar with $P_L$=10 w, $A_R$ = 1 m$^2$, $\lambda_c$ = 1 km and $T_c$ = 10 min.

Because the atmospheric density and hence the signal level decreases exponentially with increasing altitude, it is very difficult to extend Rayleigh lidar temperature measurements to high altitudes. For a fixed temperature accuracy, each factor of 10 improvement in laser power or telescope area increases the altitude by only about 2 scale heights. Because the molecular backscatter cross section is approximately proportional to $\lambda^{-4}$ ($\lambda$ is the optical wavelength), modern Rayleigh lidars use high power (10-50 W) short wavelength lasers such as frequency doubled Nd:YAG lasers operating at 532 nm or XeF excimer lasers operating at 351 nm and large telescopes (~ 1 m$^2$) to obtain temperature profiles up to about 90 km with integration times ranging from 5 min to 1 h depending on the altitude. The relatively lower power (1-5 W) long wavelength (589 nm) Na lidars are only capable of achieving useful Rayleigh temperature measurements up to about 70 km.

Another effective technique for obtaining temperature profiles near the mesopause is to observe the thermally broadened hyperfine structure of the Na $D_2$ emission line with a narrowband lidar. The Na $D_2$ resonance line is actually a Doppler broadened doublet composed of 6 hyperfine lines. Figure 3 is a plot of the resonance line as a function of wavelength for several values of temperature. As the temperature decreases the minimum between the $D_{2a}$ and $D_{2b}$ lines decreases and the peak intensities of the $D_{2a}$ and $D_{2b}$ lines increase. The ratio of the backscatter cross section at the minimum between the two peaks to the value at the $D_{2a}$ peak is a very sensitive indicator of temperature. This ratio can be measured by tuning a narrowband lidar alternately between the peak and minimum and the data used to deduce the Na temperature profile [Fricke and von Zahn, 1985]. Neuber et al. [1988] have used a variation of this technique to obtain high resolution temperature profiles of the mesopause region above Andoya, Norway (69°N, 15°E).

If we neglect saturation effects and extinction of the laser beam as it propagates through the Na layer, the Na backscatter cross section can be referred from the photocount profile by using equation (5)

$$\sigma_{\mathrm{eff}} = \frac{z^2\sigma_R\rho_a(z_R)}{z_R^2\rho_s(z)}\,\frac{\left[N_s(z) - \hat{N}_B R_L\Delta t\right]}{\left[N_R(z_R) - \hat{N}_B R_L\Delta t\right]}. \tag{90}$$

In practice saturation and extinction effects can be significant and must be taken into account in processing the Na temperature data [Simonich and Clemesha, 1983; Welsh and Gardner, 1989]. If we assume for simplicity that background noise is negligible, then the ratio of the effective

backscatter cross section at the frequency of the minimum ($f_m$) between the $D_{2a}$ and $D_{2b}$ peaks to the value at the $D_{2a}$ frequency ($f_a$) is given by

$$\frac{\sigma_{eff}(f_m)}{\sigma_{eff}(f_a)} = \frac{N_s(z,f_m)}{N_s(z,f_a)} \frac{N_R(z_R,f_a)}{N_R(z_R,f_m)} \simeq \frac{N_s(z,f_m)}{N_s(z,f_a)} . \tag{91}$$

The functional dependence of this ratio on temperature is affected by homogeneous and collisional broadening, by anomalous Zeeman splitting caused by the earth's magnetic field and by the laser line shape and line width. An excellent discussion of these effects can be found in Fricke and von Zahn [1985]. This ratio is a monotonically increasing function of temperature. It varies from approximately 0.3 for T=150 K to 0.4 for T=250 K.

The accuracy of the Na temperature measurement depends on the laser linewidth, laser tuning stability and photon noise. If the laser is tuned alternately between the $D_{2a}$ peak and the minimum between the $D_{2a}$ and $D_{2b}$ peaks, the variance of the inferred Na temperature is [She et al., 1989]

$$\text{var}[T(z)] \simeq \frac{4\Delta z \Delta t}{\lambda_c T_c} \frac{T^2(z)}{N_s(z,f_a)} . \tag{92}$$

In (92) $\Delta t$ is the total time to acquire one profile with the laser tuned to the $D_{2a}$ peak and one profile with the laser tuned to the minimum between the peaks. Normally it is twice the time required to collect a single profile.

Just as with the Rayleigh technique, the Na temperature error is inversely proportional to the photon count. If we substitute (6) and (73) into (92) and assume $\Delta t$ in (92) is twice the value specified in (6), then the standard deviation of the temperature error is

$$\text{std}[T(z)] \simeq \left[\frac{4\Delta z \Delta t}{\lambda_c T_c N_s(z)}\right]^{1/2} T(z) \sim \frac{2T(z)}{\sqrt{P_L A_R \lambda_c T_c}} e^{(z-z_0)^2/4\sigma_0^2} . \tag{93}$$

Near the mesopause the seasonal variation in temperature can be substantial. The annual mean is approximately 200 K. To achieve a measurement accuracy of 1 K at the peak of the Na layer when T = 200 K requires

$$P_L A_R \lambda_c T_c \gtrsim 2 \times 10^5 \text{ wm}^3\text{s} . \tag{94}$$

This accuracy can be achieved by using a lidar with $P_L$=1 w, $A_R$=1 m$^2$, $\lambda_c$ = 1 km and $T_c$ = 3 min. By comparison a Rayleigh lidar could achieve this same accuracy and resolution at 92 km only if $P_L A_R \sim 2 \times 10^4$ wm$^2$. The Rayleigh lidar would require a 1000 w laser and 5 m diameter telescope to achieve the same performance as the Na lidar!

## VII. PRACTICAL CONSIDERATIONS IN PROCESSING RAYLEIGH AND NA LIDAR DATA

The quality of the lidar data is influenced by many factors including background noise and variations in the laser power, laser tuning and atmospheric transmittance which can cause substantial variations in the detected signal level. These effects must be compensated so that the true variations in atmospheric density and temperature can be measured. The most common approach for compensating variations in the signal level is to normalize the photocount profiles by the photon count at an altitude free of aerosol scattering. For this technique to be most effective, the normalizing count should be large to reduce errors caused by photon noise. In some applications, the Rayleigh count is averaged over a wide altitude range (say 30-60 km) to obtain the most stable and accurate estimate of the signal level used for normalizing the profiles.

The photocount profiles must also be accurately compensated for the effects of background noise. In well-engineered lidar systems the background count rate is constant so that the noise count per range bin can be estimated by averaging the counts in high altitude range bins where the Rayleigh and Na counts are negligible. Sometimes the large signal levels at low altitudes can cause saturation and after-pulsing in the PMT so that the count rate decreases or oscillates with time (and therefore altitude). This problem can be minimized by using PMT's designed to exhibit minimum after-pulsing and by gain switching the PMT to eliminate saturation by the strong low-altitude signals. The Rayleigh temperature algorithm (equation (86)) is especially sensitive to errors in the estimated background noise level. Reliable temperature measurements can only be obtained by taking great care to insure that the background count level is properly estimated and subtracted from the photocount profiles. Data processing for Na density studies is straightforward and has been described in detail elsewhere [Gardner and Shelton, 1981; Gardner et al., 1986].

For dynamics studies, data analysis is critically dependent on the accurate computation of the relative density variations $r_a$ and $r_s$. These computations, according to equations (23) and (24), require knowledge of the unperturbed profiles or equivalently, measurements of $f_a(z)$ and $f_s(z)$. These functions can be estimated by appropriately averaging the photocount data. If we neglect background noise, equations (1), (3), (16) and (23) can be used to express the Rayleigh and Na photocount profiles in the following form

$$N(z,t) = \frac{\beta(t)}{z^2} \exp\left[-\chi - f(z-\xi)\right] \tag{95}$$

where the parameter $\beta(t)$ depends on several factors which can vary with time including laser power and atmospheric transmittance. The natural logarithm of the range-scaled photocounts is

$$\ln\left[z^2 N(z,t)\right] = \ln\beta(t) - \chi - f(z-\xi)$$

$$\simeq \ln\beta(t) - \chi - f(z) + \frac{df(z)}{dz}\xi \,. \tag{96}$$

If equation (96) is averaged over an observation period which is long compared to the correlation times of $\chi$ and $\xi_z$, the result is

$$\frac{1}{T}\int_0^T \ln\left[z^2 N(z,t)\right] dt \simeq \frac{1}{T}\int_0^T \ln\beta(t)dt - f(z) \,. \tag{97}$$

The function f(z) can now be approximated by fitting an appropriate polynomial model $\hat{f}(z)$ to equation (97). Because $\chi$ and $\xi$ are small it is just as effective (and sometimes more convenient) to average N(z,t) rather than $\ln(z^2N)$. The accuracy of the polynomial model must be significantly better than the magnitude of the actual density perturbations. For Rayleigh studies, a 3rd or 5th order polynomial in z will provide excellent fits to $f_a(z)$ depending on the observation region and period. The 3rd order fit is most effective when the altitude range and observation period are small (say < 20 km and < 4 hrs). For Na studies, a parabolic fit to $f_s(z)$ is adequate. The relative density perturbation r(z,t) is calculated by subtracting the polynomial approximation $\hat{f}(z)$ from $\ln(z^2N)$, and then computing and subtracting the spatial average to eliminate the $\ln\beta(t)$ term

$$r(z,t) = -\chi + \frac{df(z)}{dz}\xi \simeq$$

$$\ln\left[z^2 N(z,t)\right] - \hat{f}(z) - \frac{1}{L}\int_0^L \left\{ \ln\left[z^2 N(z,t)\right] - \hat{f}(z) \right\} dz \,. \tag{98}$$

A similar data processing approach can be used for Rayleigh temperature studies. To improve the accuracy of the temperature measurement it is often desirable to spatially filter the photocount profiles. If the cutoff wavelength is large (i.e., greater than a few km), filtering can severely distort the density and temperature profiles. Distortion can be avoided by filtering $r_a(z,t)$ rather than the photocounts and then computing the relative atmospheric density using equation (25)

$$\rho_a(z,t) = \exp\left[\overset{*}{r}_a(z,t) - \hat{f}_a(z)\right] \tag{99}$$

where $\overset{*}{r}_a$ denotes the filtered relative density perturbations. In the following section examples of Rayleigh and Na lidar measurements are presented.

## VIII. EXAMPLE RAYLEIGH AND NA LIDAR OBSERVATIONS OF ATMOSPHERIC DENSITY AND TEMPERATURE VARIATIONS

At mesopause heights the air is dense enough to incinerate most meteors and much of the meteoric dust that enter the atmosphere. Meteoric ablation is most pronounced between 70 and 120 km and is the major source of Na and other metals in the upper atmosphere. Although measurements are rare, lidar systems have occasionally observed the ablation trails of falling meteors. Two Na lidar profiles exhibiting returns from meteor trails are plotted in Fig. 4. These trails are typically about 100 m thick FWHM and are usually observed only for a few tens of seconds because the prevailing winds quickly advect the trails across the narrow laser beam [Beatty et al., 1988].

Typical gravity wave perturbations of the Na layer are illustrated in the density profiles plotted in Fig. 5. These perturbations are caused primarily by the vertical displacement of the layer by the vertical component of the gravity wave winds (see equation (21)). The wave activity illustrated in this figure is typical of that observed in the Na layer over Urbana at all times of the year. Monochromatic waves or events, as they are sometimes called, are usually evident during all or part of each night. The wavelengths, periods, and amplitudes of these monochromatic waves can be inferred directly from the Na layer profiles or from the spatial power spectra of the profiles [Gardner and Voelz, 1987].

Mesospheric winds, temperatures and densities are also perturbed randomly by the constructive and destructive interference of multiple waves generated by different sources. The random wind and density perturbations are best characterized statistically in terms of the gravity wave vertical wavenumber and temporal frequency spectra. Examples of temporal frequency ($\omega$) and vertical wavenumber ($k_z$) spectra inferred from lidar measurements of Na density perturbations using equations (54), (55), (69) and (71) are plotted in Figs. 6 and 7. It is common practice to plot the single-sided wind spectra in units of $(m^2s^{-2})/(cyc/m)$ or $(m^2s^{-2})/(cyc/s)$ rather than the double-sided spectra calculated in equations (69) and (71) in units of $(m^2s^{-2})/(rad/m)$ or $(m^2s^{-2})/(rad/s)$. The double-sided spectra can be converted to single-sided spectra by multiplying by 2. The wavenumber and radian frequency spectra can be converted to spatial and temporal frequency spectra by multiplying by $2\pi$. Thus the single-sided spatial and temporal frequency spectra plotted in Figs. 6 and 7 were obtained by multiplying equations (69) and (71) by $4\pi$. Theoretical analyses predict a $k_z^{-3}$ dependence for the vertical wavenumber spectrum [Dewan and Good, 1986; Smith et al., 1987]. Radar observations typically show a power law frequency dependence for the temporal spectrum with slopes ranging from -5/3 to -2 [Vincent, 1984]. Notice the enhancement of the temporal spectrum near the Brunt-Vaisala frequency. At mesopause heights, the buoyance period is approximately 5 min. The photon noise floors are clearly evident in both spectra.

Temperatures near the mesopause have been measured using a variety of techniques. Rocket launched falling spheres [Philbrick et al., 1985] and grenades [Theon et al., 1972] and airglow emissions [e.g., Sivjee and Hamwey, 1987] have all provided useful information on the temperature structure of the mesopause region. High resolution temperature profiles can also be obtained by active probing of the thermally broadened Na $D_2$ resonance line with a narrowband lidar. Although this technique was pioneered by Gibson et al. [1979] in the late 1970s, routine Na temperature observations were not attempted until von Zahn and his students from the University

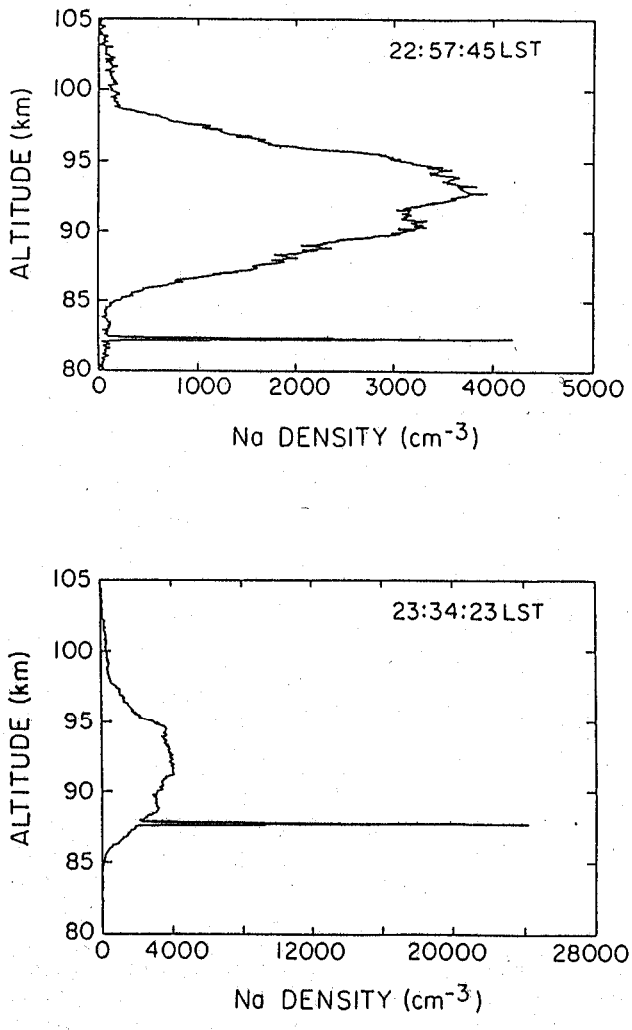


Figure 4 Na density profiles measured on March 4, 1988 at Urbana, IL. The integration period was 27s and the vertical resolution was 75 m. The dense narrow layers at 82.4 and 87 km are believed to be meteor ablation trails [Beatty et al., 1988].

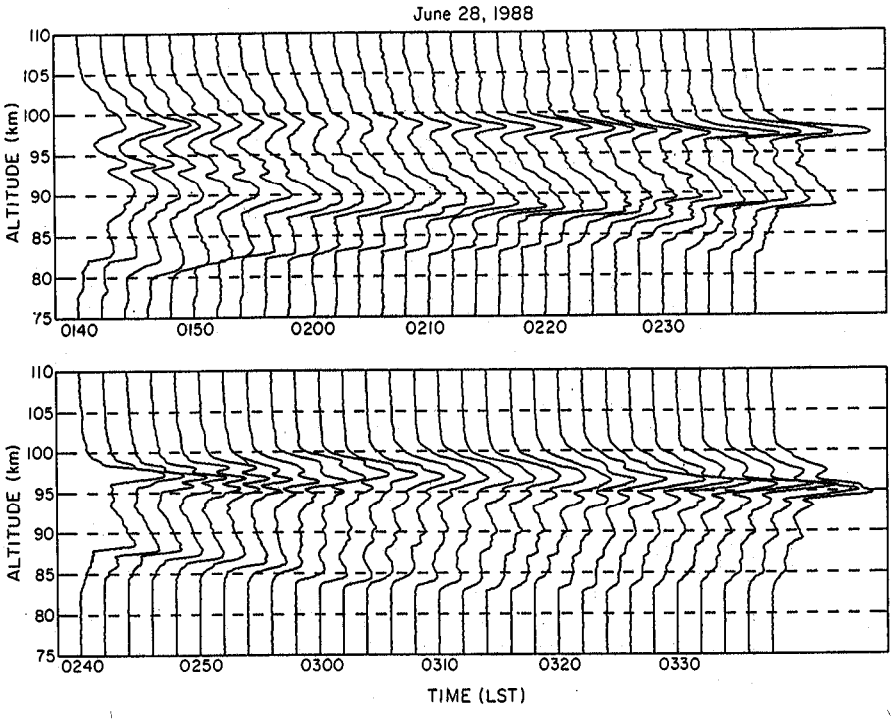


Figure 5 Na density profiles measured during the early morning of June 28, 1988 at Urbana, IL. The profiles have been plotted on a linear scale at 2 min intervals. Gravity waves are responsible for the wavelike structures in the profiles.

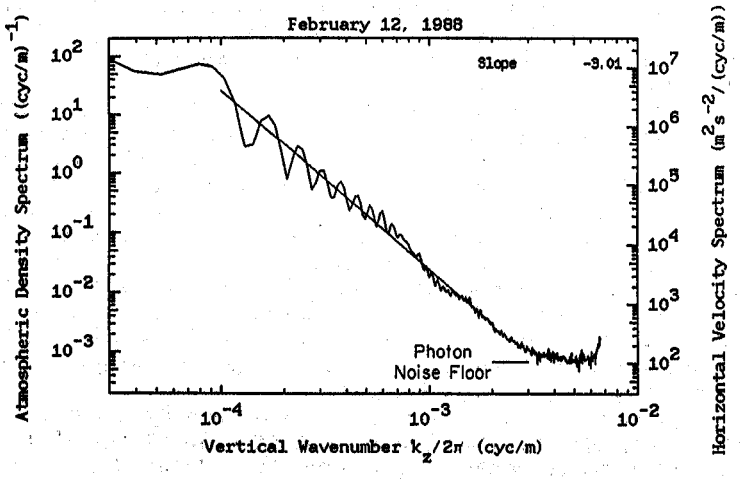


Figure 6 Vertical wavenumber spectrum of the atmospheric density and horizontal wind perturbations associated with internal gravity waves. The spectrum was inferred from Na lidar data collected between 2130 and 2330 LST on February 12, 1988 at Urbana, IL. The data were low-pass filtered temporally with a cutoff period $T_c$ = 5 min before the spectrum was computed.

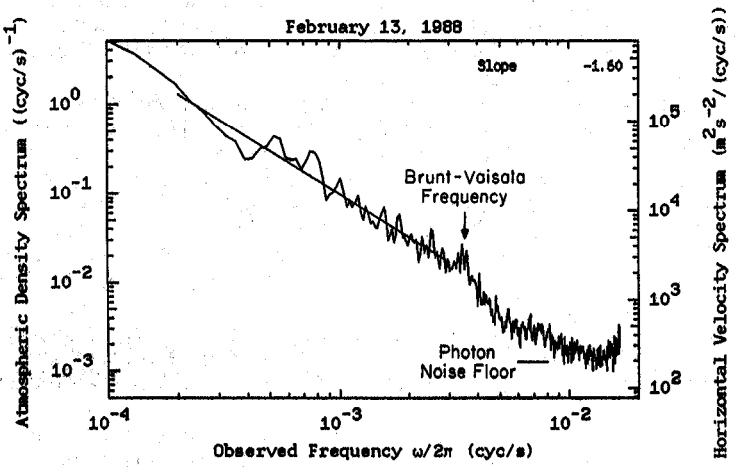


Figure 7 Temporal frequency spectrum of the atmospheric density and horizontal wind perturbations associated with internal gravity waves. The spectrum was inferred from Na lidar data collected between 0200 and 0500 LST on February 13, 1988 at Urbana,IL. The data were low-pass filtered spatially with a cutoff wavelength $\lambda_c$ = 1 km before the spectrum was computed.

of Bonn improved the laser technology and began making measurements at Andoya, Norway (69°N) during the spring of 1984 [Fricke and von Zahn, 1985]. Since then, the University of Bonn group has published several excellent lidar studies of the mesopause temperature structure above Andoya [von Zahn et al., 1987; Neuber et al, 1988].

Sodium temperature and density profiles obtained at Ft. Collins, CO on the night of August 24, 1989 are plotted in Fig. 8 [She et al., 1989]. These profiles were obtained by integrating lidar returns over a period of 5 min. The mesopause near 99 km is clearly evident. The small-scale structure in the profiles is probably caused by wave dynamics. The rms measurement error near 92 km is less than 3 K. These results clearly demonstrate the impressive capabilities of Na lidar to measure the temperature structure of the mesopause region.

Significant wave activity is also frequently seen in Rayleigh lidar observations of temperature and density profiles in the lower middle atmosphere. Figure 9 is a temperature profile calculated using equation (86) and Rayleigh lidar data collected on December 10-11, 1988 at Urbana. Because the integration period is over 9 h and the vertical resolution is 5 km, the temperature error is less than 2 K throughout the observation range. The wavelike structure in the profile is caused probably by a long period gravity wave.

Figure 10 is the vertical wavenumber spectrum of density and horizontal wind perturbations for Rayleigh lidar data collected on the night of March 8-9, 1989 at Arecibo Observatory. The spectrum was calculated using equations (70) and (54) after low-pass filtering the relative density perturbations with a cutoff frequency of $(65\ \text{min})^{-1}$. The altitude range extends from 30 to 50 km and the observation period extends from 2320 LST to 0545 LST. As we saw with the Na data, the photon noise floor is clearly evident in the spectrum as well as strong spectral peaks at $k_z/2\pi = (8.7\ \text{km})^{-1}$ and $(5.5\ \text{km})^{-1}$ which correspond to monochromatic gravity waves [Gardner et al., 1989]. The density perturbations caused by these waves are plotted versus time and altitude in Fig. 11. They were computed using the techniques described in Section VI by low-pass filtering $r_a(z,t)$. The temporal cutoff frequency was $(65\ \text{min})^{-1}$. The spatial cutoff frequencies were $(2.0\ \text{km})^{-1}$ for the top panel, $(3.75\ \text{km})^{-1}$ for the middle panel, and $(6.6\ \text{km})^{-1}$ for the bottom panel. The downward phase progression of the gravity waves is clearly evident. The relative density perturbations at 0330 LST are plotted versus altitude in Figure 12. The data were filtered temporally with a cutoff of $(65\ \text{min})^{-1}$ and spatially with a cutoff of $(2\ \text{km})^{-1}$. The perturbations increase from less than 1% at 30 km to almost 3% above 50 km.

The rms atmospheric density and wind perturbations at Arecibo Observatory for the nights of March 7-10 and 25-28, 1989 were calculated using (60) and (53). The average density profile for these eight nights is plotted versus altitude in Fig. 13. During March the density perturbations increased with altitude from approximately 1% ($\sim 4\ \text{ms}^{-1}$) at 30 km altitude to approximately 3% ($\sim 12\ \text{ms}^{-1}$) at 50 km altitude. The density and wind perturbation profiles can also be calculated from the Na data using (64) and (53). The rms atmospheric density profile calculated from Na measurements obtained at Arecibo in March 1989 is plotted in Fig. 14. This profile is the average of eight profiles measured on the same nights as the data plotted in Fig. 13. The density perturbations increased from about 2% at 80 km to about 6% near the turbopause at 100 km altitude. In fact, the decrease above 100 km suggests that for these data the turbopause may be located at 100 km altitude. The rms winds perturbations inferred from the data plotted in Figs. 13 and 14 using equations (43) and (53) are plotted in Fig. 15. The winds increase from about 4 m/s at 30 km to 25 m/s at 100 km.

The seasonal variation of gravity wave activity near the mesopause at Urbana is plotted in Fig. 16. These data were calculated by averaging the Na density perturbations throughout the layer using equations (65) and (53). The annual mean rms atmospheric density perturbation is 6.3% ($28\ \text{ms}^{-1}$). There is a semi-annual oscillation in the data with an amplitude of about 1.9% ($6\ \text{ms}^{-1}$). The maxima occur near the solstices and the minima near the equinoxes. Hirota [1984] also found evidence of a semi-annual oscillation of wave activity in the lower mesosphere by examining rocket measurements of temperature and density. At higher latitudes, an annual cycle was observed with a minimum in summertime. Radar measurements of gravity wave winds by Vincent and Fritts [1987] at Buckland Park (35°S) also show a semi-annual variation.

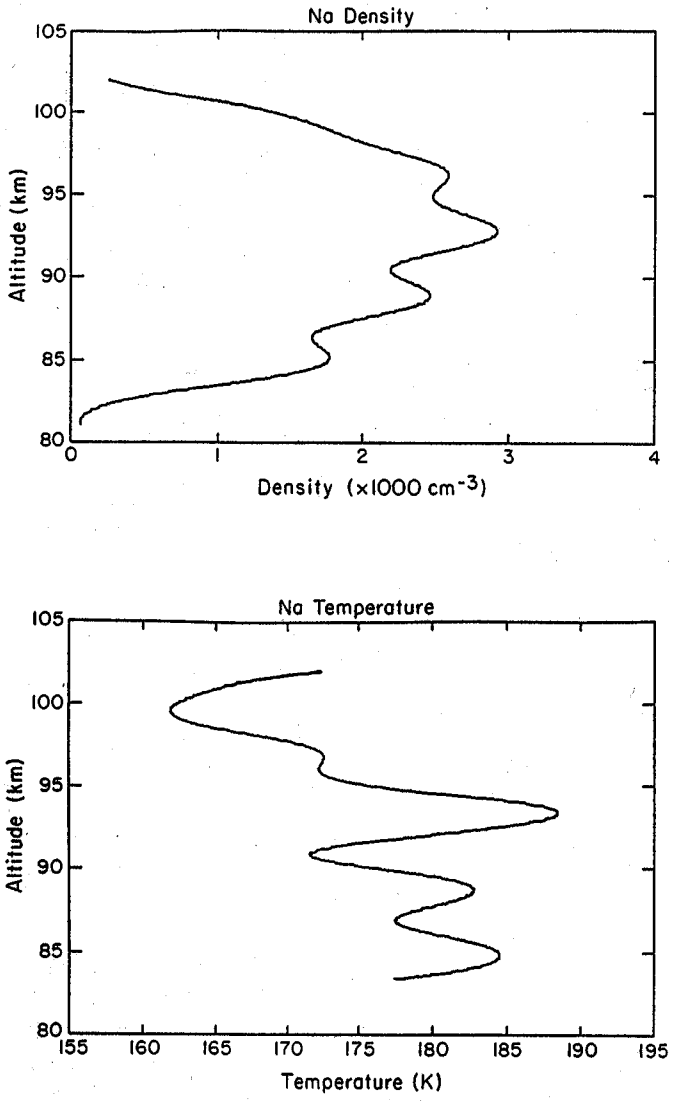


Figure 8 Na density and temperature profiles obtained at Ft. Collins, CO at 2302 LST on August 24, 1989 [She et al., 1989]. For these data $\Delta z = 1.5$ km, $\Delta T = 5$ min and the rms temperature error is less than 3 K at 92 km.

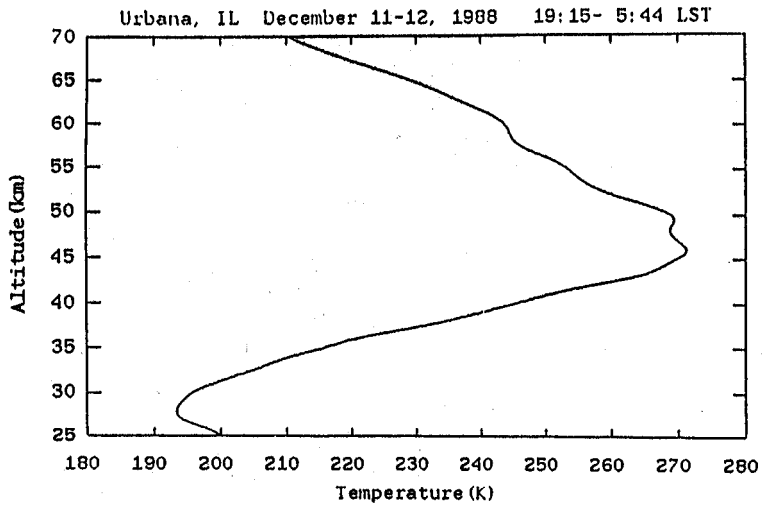


Figure 9 Temperature profile measured with a Rayleigh lidar at Urbana, IL on the night of December 10-11, 1988. For these data $\Delta z = 5$ km and $\Delta T = 9$ h 30 min. The temperature error is less than 2 K throughout the observation range.

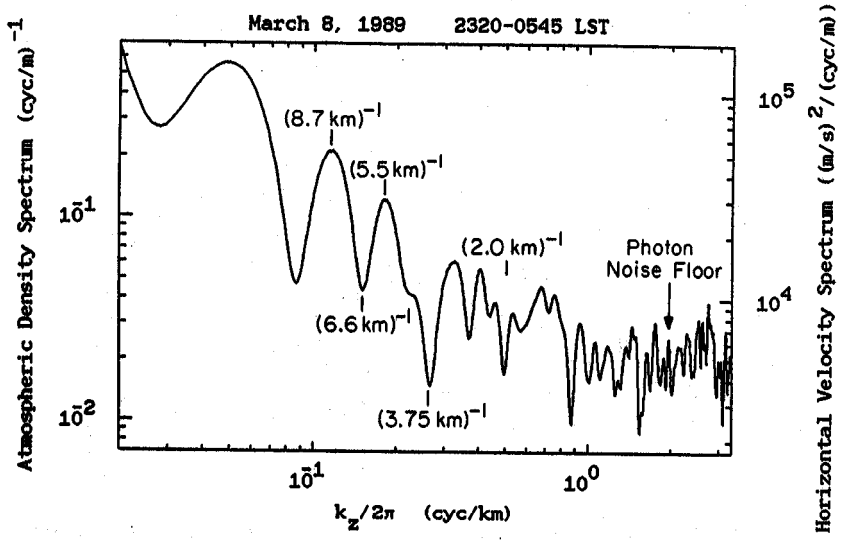


Figure 10 Vertical wavenumber spectrum of the atmospheric density and horizontal wind perturbations associated with internal gravity waves. The spectrum was inferred from Rayleigh lidar data collected between 2320 LST and 0545 LST March 8-9, 1989 at Arecibo Observatory. The data were low-pass filtered temporally with a cutoff period $T_c = 65$ min before the spectrum was computed. The altitude range is 30-50 km.

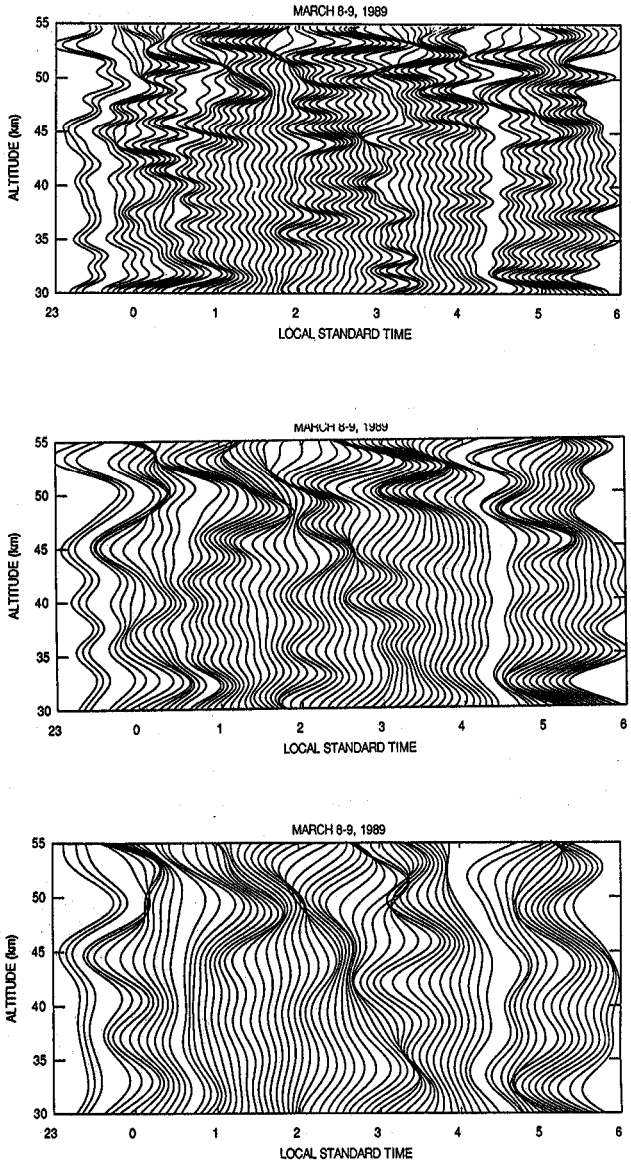


Figure 11 Altitude profiles of the relative atmospheric density perturbations measured during the night of March 8-9, 1989 at Arecibo Observatory. The data were low-pass filtered with a cutoff period $T_c$ = 65 min and cutoff wavelengths $\lambda_c$ = 2.0 km for the top panel, $\lambda_c$ = 3.75 km for the middle panel and $\lambda_c$ = 6.6 km for the bottom panel. The vertical wavenumber spectrum for these data is plotted in Fig. 10.

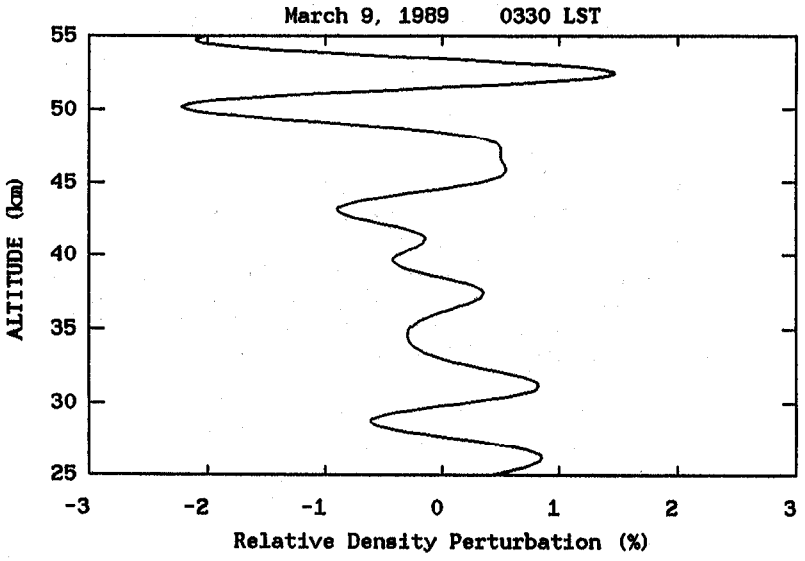


Figure 12 Altitude profile of the atmospheric relative density perturbations measured at 0330 LST on March 9, 1989 at Arecibo Observatory. The data were low-pass filtered with $\lambda_c = 2.0$ km and $T_c = 65$ min.

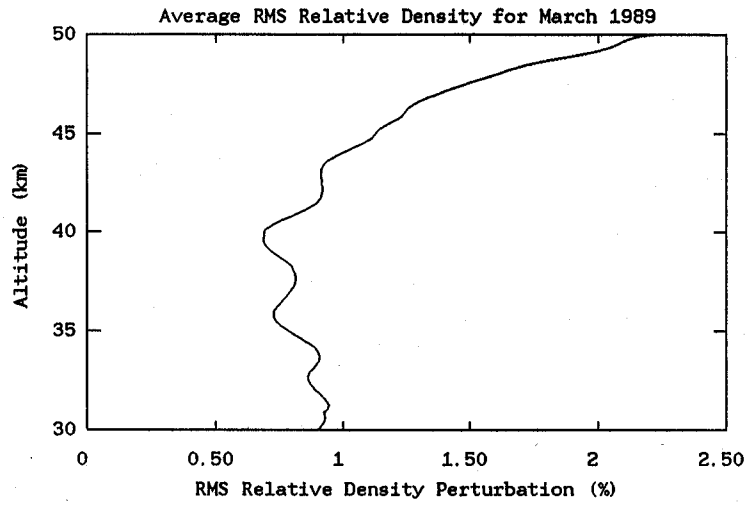


Figure 13 Altitude profile of the rms atmospheric density perturbations referred from Rayleigh lidar measurements obtained during March 1989 at Arecibo Observatory. The profile is the average of 8 nights' observations. All data were low-pass filtered with $\lambda_c = 2$ km and $T_c = 60$ min before the rms perturbations were computed.

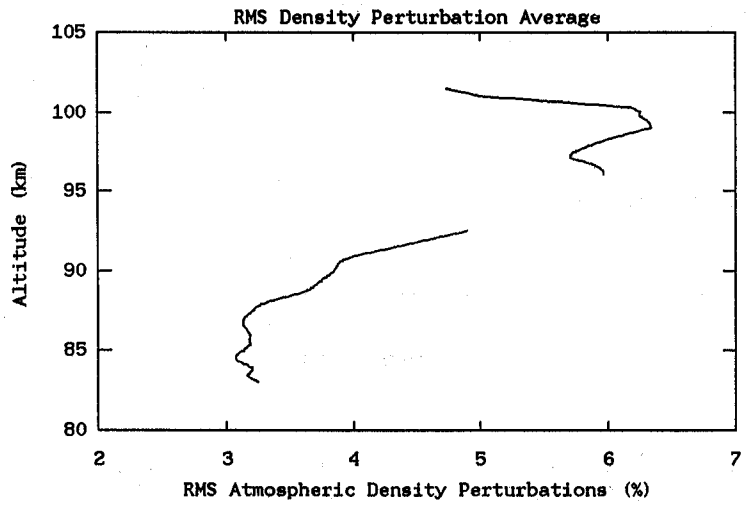


Figure 14 Altitude profile of the rms atmospheric density perturbations inferred from Na lidar measurements obtained during March 1989 at Arecibo Observatory. The profile is the average of observations obtained during the same 8 nights used to compute the data plotted in Figure 13. All data were low-pass filtered with $\lambda_c = 1$ km and $T_c = 5$ min before the rms perturbations were computed.

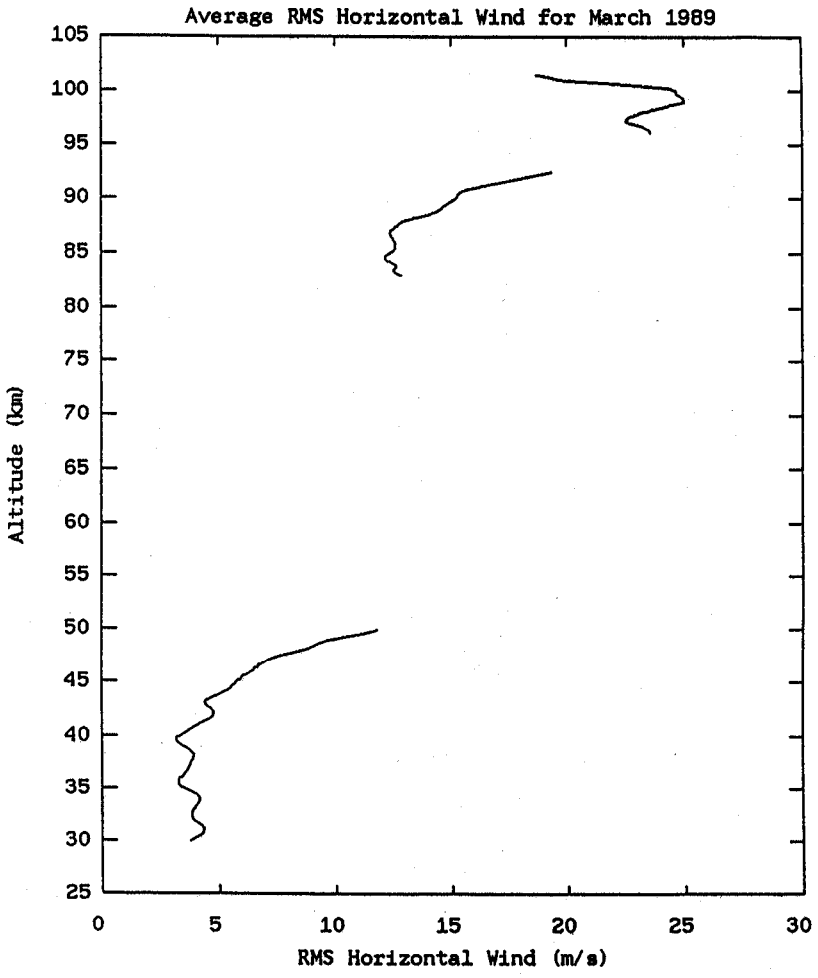


Figure 15 Altitude profile of the rms horizontal wind perturbations inferred from Rayleigh and Na lidar measurements obtained during March 1989 at Arecibo Observatory. The profile was inferred from the data plotted in Figures 13 and 14 by using equations (43) and (53).

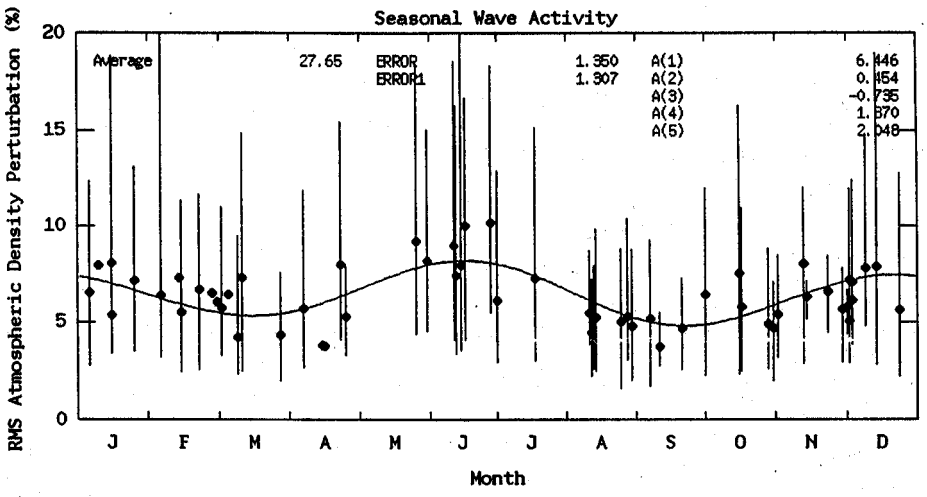


$$\rho_{rms}\ (\%) = 6.45 + 0.454 \sin\left[\frac{2\pi}{365}(d-43)\right] + 1.87 \sin\left[\frac{4\pi}{365}(d+59)\right]$$

d = day number

Figure 16 Seasonal variation of the rms atmosphere density perturbations at Urbana, IL. The data were obtained in 1986-89. The lines are the range of values measured during the night and the dots denote the average value for the night. The solid curve is the least-squares annual plus semi-annual variation.

## IX. CONCLUSIONS

Rayleigh and Na lidars are perhaps best suited for studying the vertical and temporal structure of the middle atmosphere. Modern Na lidars can achieve vertical resolutions of a few tens of meters with temporal resolutions of a few tens of seconds. Although the signal levels for Rayleigh lidars are weaker, in the upper stratosphere modern Rayleigh lidars can achieve vertical and temporal resolutions of a few hundred meters and a few minutes respectively. Lidars are attractive remote sensing instruments because they are portable and don't require extensive support facilities for their operation. In fact, airborne Na lidar measurements have been reported [Kwon et al., 1989], and several spaceborne systems have been proposed [Yeh and Browell, 1982; Philbrick et al., 1985]. Spaceborne systems are especially attractive because they can provide global measurements of gravity wave and tidal activity and can be used to study the horizontal structure of these important wave phenomena. Currently there is a significant lack of observational data on the climatology and horizontal characteristics of both gravity waves and tides. In addition very little is known about the geographical distribution and characteristics of gravity wave sources. Airborne and satellite based Rayleigh and Na lidars can help provide that information.

Although most of our observational knowledge of middle atmosphere winds has been obtained with radars, only lidars can provide high resolution measurements of the atmospheric density and temperature. Rayleigh and Na lidars are mature techniques that are being used routinely to observe these parameters in the upper stratosphere, mesosphere and lower thermosphere. In this paper we have reviewed the capabilities Rayleigh and Na lidar systems for measuring temperature, density and wind perturbations and the spatial and temporal spectra of these important parameters. The results clearly demonstrate the potential of these two lidar techniques and illustrate the critical importance of laser power and telescope area in determining the quality of the observations.

*Acknowledgements*. The authors gratefully acknowledge the many helpful discussions with colleagues C. H. Liu and S. F. Franke at the University of Illinois, C. Y. She at Colorado State University, J. W. Meriwether at the Geophysics Laboratory and C. R. Philbrick at Pennsylvania State University. Some of the data presented here were obtained during the AIDA Act 89 Campaign at Arecibo. We thank Colin Hines for inviting us to participate in this campaign as part of the NSF CEDAR Program. We also acknowledge the excellent support and assistance provided by C. A. Tepley at Arecibo. We thank Nina Parsons for the superb job she did in preparing the manuscript. This work was supported in part by grants from the National Science Foundation and the Air Force Geophysics Laboratory.

## REFERENCES

Batista, P. P., B. R. Clemesha, D. M. Simonich and V. W. J. H. Kirchhoff, Tidal oscillations in the atmospheric sodium layer, *J. Geophys. Res.*, *90*, 3881-3888, 1985.

Beatty, T. J., R. E. Bills, K. H. Kwon and C. S. Gardner, CEDAR lidar observations of sporadic Na layers at Urbana, Illinois, *Geophys. Res. Lett.*, *15*, 1137-1140, 1988.

Chanin, M., and A. Hauchecorne, Lidar observation of gravity and tidal waves in the stratosphere and mesosphere, *J. Geophys. Res.*, *86*, 9715-9721, 1981.

Dewan, E. M., and R. E. Good, Saturation and the "universal" spectrum for vertical profiles of horizontal scalar winds in the atmosphere, *J. Geophys. Res.*, *91*, 2742-2748, 1986.

Elterman, L. B., The measurement of stratospheric density distribution with the search light technique, *J. Geophys. Res.*, *56*, 509-520, 1951.

Elterman, L. B., A series of stratospheric temperature profiles obtained with the searchlight technique, *J. Geophys. Res.*, *58*, 519-530, 1953.

Elterman, L. B., Seasonal trends of temperature, density and pressure to 67.6 km obtained with the searchlight probing technique, *J. Geophys. Res.*, *59*, 351-358, 1954.

Fricke, K. H., and U. von Zahn, Mesopause temperature derived from probing the hyperfine structure of the $D_2$ resonance line of sodium by lidar, *J. Atmos. Terr. Phys.*, *47*, 499-512, 1985.

Fritts, D. C., Gravity wave saturation in the middle atmosphere: A review of theory and observations, *Rev. Geophys.*, *22*, 275-308, 1984.

Gardner, C. S., M. S. Miller and C. H. Liu, Rayleigh lidar observations of gravity wave activity in the upper stratosphere at Urbana, Illinois, *J. Atmos. Sci.*, *46*, 1838-1854, 1989.

Gardner, C. S., and J. D. Shelton, Spatial and temporal filtering technique for processing lidar photocount data, *Opt. Lett.*, *6*, 174-176, 1981.

Gardner, C. S., and J. D. Shelton, Density response of neutral atmospheric layers to gravity wave perturbations, *J. Geophys. Res.*, *90*, 1745-1754, 1985.

Gardner, C. S., and D. G. Voelz, Lidar Studies of the nighttime sodium layer over Urbana, Illinois 2. Gravity waves, *J. Geophys. Res.*, *92*, 4673-4694, 1987.

Gardner, C. S., D. G. Voelz, C. F. Sechrist, Jr., and A. C. Segal, Lidar Studies of the nighttime sodium layer over Urbana, Illinois, 1, Seasonal and nocturnal variations, *J. Geophys. Res.*, *91*, 13659-13673, 1986.

Gibson, A., L. Thomas and S. Bhattachacharyya, Lidar observations of the ground-state hyperfine structure of sodium and of temperatures in the upper atmosphere, *Nature*, *281*, 131-132, 1979.

Hirota, L., Climatology of gravity waves in the middle atmosphere, *J. Atmos. Terr. Phys.*, *46*, 767-773, 1984.

Iwasaka, Y., T. Ono, and A. Nomura, Changes in aerosol content and temperature in the Antarctic spring stratosphere; Lidar measurement at Syowa Station (69°00'S, 39°35'E) in 1983, 1984, and 1985, *Geophys. Res. Lett.*, *13*, 1407-1410, 1986.

Kent, G. S., L. R. Poole, and M. P. McCormick, Characteristics of arctic polar stratospheric clouds as measured by airborne lidar, *J. Atmos. Sci.*, *43*, 2148-2161, 1986.

Kwon, K. H., C. S. Gardner, D. C. Senft, F. L. Roesler, and J. Harlander, Daytime lidar measurements of tidal winds in the mesospheric sodium layer at Urbana, Illinois, *J. Geophys. Res.*, *92*, 8781-8786, 1987.

Kwon, K. H., D. C. Senft, and C. S. Gardner, Airborne sodium lidar observations of horizontal and vertical wavenumber spectra of mesopause density and wind perturbations, *J. Geophys. Res.*, in press, 1989.

Lindzen, R. S., Turbulence and stress owing to gravity wave and tidal breakdown, *J. Geophys. Res.*, *86*, 9707-9714, 1981.

McCormick, M. P., T. J. Swissler, W. H. Fuller, W. H. Hunt, and M. T. Osborn, Airborne and groundbased lidar measurements of the El Chichon stratospheric aerosol from 90°N to 56°S, *Geof. Inst.*, *23*, 198-221, 1984.

Neuber, R., P. von der Gathen, and U. von Zahn, Altitude and temperature of the mesopause at 69°N latitude in winter, *J. Geophys. Res.*, *93*, 11,093-11,101, 1988.

Philbrick, C. R., J. L. Bufton, and C. S. Gardner, A solid state tunable laser for resonance measurements of atmospheric sodium, in *Tunable Solid State Lasers for Remote Sensing, Ser. Opt. Sci.*, vol. 51, R. L. Byer, E. K. Gustafson, and R. Trebino, Eds. New York, NY: Springer-Verlag, 1985, pp. 42-46.

Philbrick, C. R., et al., Density and temperature structure over northern Europe, *J. Atmos. Terr. Phys.*, *47*, 159, 1985.

Reiter, R., and H. Jager, Results of 8-year continuous measurements of aerosol profiles in the stratosphere with discussion of the importance of stratospheric aerosols to an estimate of global climates, *Meterol. Atmos. Phys.*, *35*, 19-48, 1986.

She, C. Y., R. E. Bills, H. Latifi, J. R. Yu, B. J. Alvarez II and C. S. Gardner, Two-frequency lidar technique for mesospheric Na temperature measurements, *Geophys. Res. Lett.*, in press, 1989.

Simonich, D. M., and B. R. Clemesha, Resonant extinction of the lidar returns from the alkalai metal layers in the upper atmosphere, *Appl. Opt.*, *22*, 1387-1389, 1983.

Sivjee, G. G., and R. M. Hamwey, Temperature and chemistry of the polar mesopause OH, *J. Geophys. Res.*, *92*, 4663, 1987.

Smith, S. A., D. C. Fritts, and T. E. VanZandt, Evidence of a saturated spectrum of atmospheric gravity waves, *J. Atmos. Sci.*, *44*, 1404-1410, 1987.

Theon, J. S., et al., The mean observed structure and circulation of the stratosphere and mesosphere, NASA Tech. Rep. TR-375, Mar. 1972.

Vincent, R. A., Gravity wave motions in the mesosphere, *J. Atmos. Terr. Phys.*, *46*, 119-128, 1984.

Vincent, R. A., and D. A. Fritts, A climatology of gravity wave motions in the mesopause region at Adelaide, Australia, *J. Atmos. Sci.*, *44*, 748-760, 1987.

von Zahn, U., K. H. Fricke, R. Gerndt and T. Blix, Mesopheric temperatures and the OH layer height as derived from ground-based lidar and OH spectrometry, *J. Atmos. Terr. Phys.*, *49*, 863-869, 1987.

Welsh, B. M., and C. S. Gardner, Nonlinear resonant absorption effects on the design of resonance fluorescence lidars and laser guide stars, *Appl. Opt.*, *28*, 4141-4153, 1989.

Yeh, S., and E. V. Browell, Shuttle lidar resonance fluorescence investigations, 1, Analysis of Na and K measurements, *Appl. Opt.*, *21*, 2365-2372, 1982.